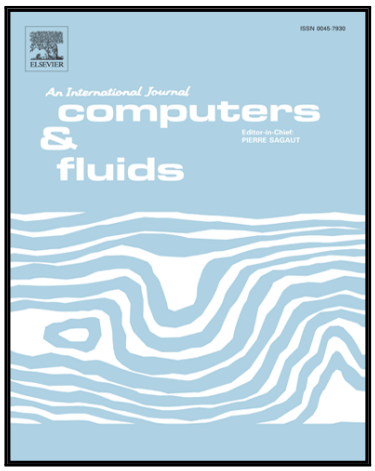

A Low-Dissipation Convection Scheme for the Stable Discretization of Turbulent Interfacial Flow

Eugenio Schillaci, Lluís Jofre, Néstor Balcázar, Oscar Antepara, Assensi Oliva

PII: S0045-7930(17)30169-X
DOI: 10.1016/j.compfluid.2017.05.009
Reference: CAF 3479

To appear in: *Computers and Fluids*

Received date: 27 December 2016
Revised date: 22 April 2017
Accepted date: 12 May 2017

Please cite this article as: Eugenio Schillaci, Lluís Jofre, Néstor Balcázar, Oscar Antepara, Assensi Oliva, A Low-Dissipation Convection Scheme for the Stable Discretization of Turbulent Interfacial Flow, *Computers and Fluids* (2017), doi: 10.1016/j.compfluid.2017.05.009

Highlights

- Analysis of a low-dissipation scheme for the DNS of turbulent two-phase flow.
- Introduction of a stabilizing hybrid convection scheme for the momentum equations.
- Kinetic energy conservation in each phase improves simulation of turbulent flow.
- Spurious currents in large density ratio problems are minimized.
- Adaptable to different interface-capturing methods, as VOF and Level-Set.

A Low-Dissipation Convection Scheme for the Stable Discretization of Turbulent Interfacial Flow

Eugenio Schillaci*, Lluís Jofre, Néstor Balcázar, Oscar Antepara, Assensi Oliva*

Heat and Mass Transfer Technological Center (CTTC), Universitat Politècnica de Catalunya - BarcelonaTech (UPC), ESEIAAT, Colom 11, E-08222 Terrassa, Barcelona, Spain

Abstract

This paper analyzes a low-dissipation discretization for the resolution of immiscible, incompressible multiphase flow by means of interface-capturing schemes. The discretization is built on a three-dimensional, unstructured finite-volume framework and aims at minimizing the differences in kinetic energy preservation with respect to the continuous governing equations. This property plays a fundamental role in the case of flows presenting significant levels of turbulence. At the same time, the hybrid form of the convective operator proposed in this work incorporates localized low-dispersion characteristics to limit the growth of spurious flow solutions. The low-dissipation discrete framework is presented in detail and, in order to expose the advantages with respect to commonly used methodologies, its conservation properties and accuracy are extensively studied, both theoretically and numerically.

*Corresponding author. Tel.: +34 93 739 81 92; Fax: +34 93 739 89 20.
Email addresses: eugenio@cttc.upc.edu (Eugenio Schillaci), cttc@cttc.upc.edu (Assensi Oliva)

Numerical tests are performed by considering a three-dimensional vortex, an exact sinusoidal function, and a spherical drop subjected to surface tension forces in equilibrium and immersed in a swirling velocity field. Finally, the turbulent atomization of a liquid-gas jet is numerically analyzed to further assess the capabilities of the method.

Keywords: low-dissipation/low-dispersion scheme, stabilizing hybrid convection scheme, interface-capturing method, turbulent interfacial flow, two-phase atomization

1. Introduction

Multiphase immiscible flow refers to any fluid flow consisting of two or more phases incapable of being mixed to form a homogeneous substance. Theoretically, this kind of flow should be regarded as multi-fluid flow, but it is often referred to as multiphase flow due to their similarity in behavior [1]. Consequently, the flows considered exhibit phase separation at a scale well above the molecular level. Generally, these flows are categorized depending on the components distribution: disperse or separated. The disperse flow consists of finite particles, drops or bubbles distributed in a connected volume of the continuous phase, whereas the separated case refers to the situation in which two or more continuous streams of different phases are separated by interfaces. This paper is focused on the latter situation.

The case of phases separated by interfaces, also referred to as interfacial flow, is found in a large variety of physical and biological phenomena, ranging

from the prediction of atmospheric conditions to the study of blood flow, and in many engineering applications, like for example, cavitation in pumps and turbines, bubbly flows, sprays or injection processes. Understanding the flow in these situations not only involves the study of velocity and pressure in the different phases, i.e., resolution of mass and momentum balances, but also of the dynamics of the interface separating them. Therefore, its correct representation and coupling to the equations of fluid motion add several complexities to the solution of the problem.

1.1. Governing equations

Interfacial flows are governed by the mass and momentum equations in the variable-density incompressibility limit, written in divergence form as [2, 3]

$$\nabla\cdot\mathbf{u} = 0, \tag{1}$$

$$\frac{\partial(\rho\mathbf{u})}{\partial t} + \nabla\cdot(\rho\mathbf{u}\mathbf{u}) = -\nabla p + \nabla\cdot\left[\mu(\nabla\mathbf{u} + \nabla^{\intercal}\mathbf{u})\right] + \rho\mathbf{g} + T_\sigma, \tag{2}$$

where $\mathbf{u}$ and p represent velocity and pressure, $\rho\mathbf{g}$ accounts for the gravitational acceleration, and T_σ is the interfacial surface tension force evaluated as

$$\mathbf{T}_\sigma = \sigma\kappa\mathbf{n}_\Gamma\delta(\mathbf{x}-\mathbf{x}_\Gamma), \tag{3}$$

with σ the constant surface tension coefficient, κ and $\mathbf{n}_\Gamma$ the curvature and unit normal vector of the interface, respectively, and $\delta(\mathbf{x}-\mathbf{x}_\Gamma)$ the Dirac delta

function concentrating the force in the interface region. The peculiarity of this system of equations is found in the evaluation of density ρ, and dynamic viscosity μ, since they are calculated according to the location of the interface Γ, interpolating them from the properties of each phase k by means of phase-volume fraction values C_k written as

$$\rho = \sum_k C_k \rho_k \quad \text{and} \quad \mu = \sum_k C_k \mu_k. \tag{4}$$

1.2. Full-domain modelization

The location of the interface determines a discontinuity in density and viscosity, as well as in other physical variables, and is considered to be, in three-dimensions (3-D), a smooth surface that links the different phases by transferring momentum between them. In the case of negligible phase change, an interface evolves according to the velocity field as

$$\frac{d\mathbf{x}_\Gamma}{dt} = \mathbf{u}(\mathbf{x}_\Gamma, t), \tag{5}$$

where $\mathbf{x}_\Gamma$ refers to the points on the interface between phases. As introduced in the work by Scardovelli and Zaleski [4], many different methods exist to numerically solve Eq. 5. Among the various possibilities, this work chooses the interface-capturing approach, which employs one set of equations to describe the different phases instead of utilizing one for each subdomain k. This methodology allows the spatial discretization of the entire domain on a single static grid, while the interface is captured by means of scalar functions. The

main advantage is that large interface distortions, e.g., due to strong swirling flows, are properly handled, avoiding the necessity to continuously adapt the mesh to a varying interface topology. This is pointed out for instance by Gorokhovski and Herrmann [5] in the context of multiphase jets.

The two main interface-capturing options are the Volume-of-Fluid (VOF) [6, 7, 8, 9] and Level-Set (LS) [10, 11, 3] methods. Therefore, to properly assess the performance of the low-dissipation scheme proposed, both approaches are considered in the numerical tests section. These two approaches mainly differ in the choice of the scalar fields C_k, also referred to as indicator functions, used to capture the motion of each phase k within the domain. The indicator function is advected by means of a transport equation, which in the hypothesis of immiscibility of fluids and divergence-free velocity fields, i.e., $\nabla\cdot\mathbf{u}=0$, reads

$$\frac{\partial C_k}{\partial t}+\nabla\cdot(C_k\mathbf{u})=0, \tag{6}$$

where a unique velocity field, i.e., $u^k=\mathbf{u}$, has been considered for all phases. In the VOF method, the advected function is the phase-volume fraction C_k, defined as the portion of volume filled by each phase k, and expressed as

$$C_k(\mathbf{x},t)=\frac{1}{V_\Omega}\int_\Omega H(\mathbf{x}-\mathbf{x}_\Gamma)d\mathbf{x}, \tag{7}$$

where H is the Heaviside function. The obtainment of the C_k scalar values by means of solving Eq. 6 provides closure to the evaluation of the varying density and dynamic viscosity properties, Eq. 4, across the whole domain, and

at the same time provides the interface topology required for the evaluation of capillary stresses. As detailed in previous works by Jofre et al. [8, 9], the VOF method provides an implicit volume-preserving formulation, however, due to its geometrical nature, the process of advancing volume fraction values in time can be rather time-consuming when good accuracy is required [12]. In the LS method, C_k is a regularized level-set function where the interface is defined as the set of points for which the function equals 0.5. Particularly, following the method proposed by Balcázar et al. [3], C_k is evaluated for each phase as

$$C_k(\mathbf{x},t) = \frac{1}{2}\left[\tanh\left(\frac{d(\mathbf{x},t)}{2\varepsilon}\right) + 1\right], \tag{8}$$

where $d(\mathbf{x},t)$ is the signed distance function from the interface and ε is a parameter controlling the interface thickness. In order to maintain the interface sharp, C_k is re-initialized after the advection step according to the following equation

$$\frac{\partial C_k}{\partial \tau} + \nabla \cdot C_k(1-C_k)\mathbf{n} = \nabla \cdot \varepsilon \nabla C_k, \tag{9}$$

where τ is the re-initialization pseudo-time. The main drawback of the standard LS method [10] is that it is not strictly conservative, as the volume bounded by the interface contour is not conserved exactly when advected and re-initialized — several strategies have been proposed to minimize this drawback [11, 3, 12]. Besides, due to the continuity of the level-set function, the values of viscosity and density of the fluids in contact vary smoothly

across the interface. This enhances the numerical stability of the algorithm, albeit it is an artificial continuous representation of the sharp interface separating the different phases.

As previously introduced, full-domain modelizations embed the different phases within a single static mesh. This procedure may result, especially in problems presenting large density ratios, in the appearance of parasitic flows, or spurious currents, close to the interfaces due to the continuous treatment of an inherent discontinuous mathematical description. These unphysical flows are produced by imbalances between the discrete representation of pressure gradients and capillary forces in the variable density zone. As a consequence, fluids may be artificially accelerated at the interface resulting in poor mass conservation, and consequently failure to properly represent the interface topology. As concluded by Lafaurie et al. [13] and Renardy and Renardy [14], the magnitude of parasitic flows scales with the inverse of the capillary number, and it may not decrease with mesh refinement. Zahedi et al. [15] comprehensively analyzed the effect of several factors on spurious currents, concluding that, when using a regularized force method for the discretization of capillary forces, the most influential parameter is the numerical evaluation of interface curvature. Other authors managed to reduce the presence of interfacial spurious currents by studying in detail the causes that originate them [16], and by proposing improved discretizations of the pressure gradient and surface tension force [17, 18].

The appearance of spurious currents in the discrete solution of interfa-

cial flows presenting large density ratios is also related to the complexity of ensuring mass conservation at the interface region. For instance, in the case of solving the velocity-pressure coupling of the momentum equations by means of a projection method, e.g., fractional-step method [19], a variable-coefficient Poisson's pressure linear system must be solved at each time step. The ill-posedness of the resulting linear system due to the discontinuity in density across the interface complicates its resolution with high accuracy. As a result, the projection of the predicted velocity field onto a divergence-free space, i.e., $\nabla \cdot \mathbf{u}$, by means of the pressure gradient is difficult to achieve to machine precision with a relatively low computational cost. This turns out in the appearance of spurious velocities that propagate from the high- to the low-density phase. A solution often considered is to deactivate the light phase and impose a specific pressure at the free surface. This methodology is known as single-phase model [20, 21, 22], and leads to stabler behaviors since the spurious currents can be eliminated by construction. However, although practical for a wide range of free-surface flows —e.g., sea waves or water impact problems—, this simplification is not a general solution for interfacial flow.

1.3. Objectives and outline

Consideration of secondary discrete conservation properties, such as kinetic energy or vorticity, for the development of numerical schemes has barely been a priority in the multiphase literature, and pure dissipative models have

been widely used in many reference works [23, 24, 25]. This is in contrast with the path taken by the single-phase turbulent community [26, 27, 28], which has evolved to discretely preserve mass, momentum and, specifically, kinetic energy by using skew-symmetric formulations at expenses of increasing the local truncation error. To the best of the authors' knowledge, only the recent work by Fuster [29] explicitly proposes the use of kinetic-energy-preserving schemes for the discretization of interfacial phenomena on 3-D Cartesian grids.

The absence of artificial numerical dissipation enhances the correct resolution of turbulent flows by mimicking the conservation properties of the continuous governing equations, where dissipation is restricted to the enstrophy term. However, as demonstrated in Sec. 5, potential non-physical flows originated during the discrete advancement of the conservation equations may grow unlimited due to the incapacity of the numerical framework to counteract them. This is of paramount importance in the case of interfacial flows presenting large density ratios between phases, in which full-domain modelizations usually propitiate the appearance of spurious currents at the interfaces. In this regard, the current work aims at developing a low-dissipation convective scheme for interfacial turbulent flow that prioritizes the conservation of kinetic energy, while at the same time presents low-dispersion characteristics at the interface regions. The numerical framework analyzed is suitable for both unstructured and Cartesian 3-D meshes, with the enhanced feature that the interface resolution of the latter can be

improved with dynamic refinement strategies.

Particular attention is given to the convection term in the Navier-Stokes equations due to its role in the transfer of energy between turbulent scales. In detail, the work proposes the utilization of a hybrid convection scheme: conservative in the bulk of the phases, whereas stabilizing at the interface regions. The conservative convection scheme chosen is the symmetry-preserving [26], characterized by the conservative transport of kinetic energy between turbulent scales — this property is fundamental for the correct resolution of turbulence [27]. On the other hand, the low-dispersion convection scheme selected is the one presented by Veldman and Lam [30], which guarantees that the resulting discrete convective matrix operator is positive-definite, i.e., extracts energy out of the system.

Alike strategies have been proposed for other types of physics. For example, it is commonly used for capturing shock waves in compressible flows. In that context, different authors have proposed hybridization of conservative and discontinuity-capturing convection schemes that reduce numerical dissipation while maintain the ability to capture shocks — a general overview of such methods is proposed by Pirozzoli [31]. A common feature of all these hybrid frameworks is the role played by the position sensors. In compressible flow, their purpose is to limit the activation of the low-dispersion scheme just to the shocked regions, without affecting the rest of the flow field. Similarly, the position sensors in this work will be utilized to stabilize only the interface regions.

Therefore, this paper presents and analyzes a low-dissipation and low-dispersion discrete framework for the numerical simulation of interfacial turbulent flow on 3-D unstructured meshes. The remaining part of the document is organized as follows. A detailed description of the proposed numerical method is presented in Sec. 2. Analysis of the discrete conservation properties is given in Sec. 3. Complementing the two previous sections, Sec. 4 presents and analyzes the hybrid convection scheme proposed. Finally, numerical tests are performed in Sec. 5 and conclusions are drawn in Sec. 6.

2. Discrete Navier-Stokes equations

The continuity and Navier-Stokes equations governing interfacial flow, Eqs. 1 and 2, are discretized over unstructured meshes by means of a collocated approach —staggered schemes present enhanced conservation properties but suffer from low accuracy on 3-D unstructured meshes. In a general context, collocated mesh discretizations, independently of the time integration chosen, calculate velocity and pressure at cell centers, whereas mass fluxes and other variables evaluated at cell faces require specific interpolations in order to exactly satisfy the mass constraint and preserve physical properties. The scheme is based on the one extensively analyzed by Jofre et al. [27] for incompressible single-phase flow, and the finite-volume discretization of two-phase flow with surface tension introduced by Balcázar et al. [3]. In this section the discretization process is reviewed in detail.

The numerical framework analyzed solves the velocity-pressure coupling

of the momentum equations, Eq. 2, by means of a fractional step projection method [19] along with a first-order explicit time advancement — higher order temporal schemes can be used, but for clarity the first-order one is chosen—, written as

$$\rho^{n+1}\mathbf{u}^{n+1} - \rho^{n+1}\mathbf{u}^{p} = -\Delta t \nabla p^{n+1}, \tag{10}$$

$$\rho^{n+1}\mathbf{u}^{p} = \rho^{n}\mathbf{u}^{n} - \Delta t \left[\nabla\cdot(\rho^{n}\mathbf{u}^{n}\mathbf{u}^{n}) - \nabla\cdot\left[\mu^{n}(\nabla\mathbf{u}^{n} + \nabla^{\intercal}\mathbf{u}^{n})\right] - \mathbf{S}^{n+1}\right], \tag{11}$$

where the superscript n refers to time instant, $\mathbf{u}^{p}$ is the predictor velocity, Δt is the time step, and $\mathbf{S}$ is a source term including the different forces.

First, the predictor discrete velocity is obtained by dividing Eq. 11 by density, ρ^{n+1}, integrating over a cell c, and applying the divergence theorem to its bordering faces $f \in F(c)$, resulting in

$$\begin{aligned}\mathbf{u}_{c}^{p} =& \frac{\rho_{c}^{n}\mathbf{u}_{c}^{n}}{\rho_{c}^{n+1}} - \frac{\Delta t}{\rho_{c}^{n+1}V_{c}}\sum_{f\in F(c)}\boldsymbol{\phi}_{f}^{n}\hat{M}_{f}^{n} \\ &+ \frac{\Delta t}{\rho_{c}^{n+1}V_{c}}\left[\sum_{f\in F(c)}\mu_{f}^{n}\left[(\mathbf{u}_{nb}^{n} - \mathbf{u}_{c}^{n})\frac{A_{f}}{\delta d_{f}} + \nabla^{\intercal}\mathbf{u}_{f}^{n}\cdot\hat{\mathbf{n}}_{f}A_{f}\right]\right] + \frac{\Delta t}{\rho_{c}^{n+1}V_{c}}\mathbf{S}_{c}^{n+1}V_{c},\end{aligned} \tag{12}$$

where V_c is the volume of cell c, $\boldsymbol{\phi}_f$ is the convected velocity at face f, $\hat{M}_f$, $\hat{\mathbf{n}}_f$ and A_f are the outward mass flux, the normal outward unit vector and the surface of face f, respectively, subscript nb refers to the neighbor cells sharing a face with cell c, length δd_f is the normal-projected distance between the centroids of cells c and nb, and the viscous term is discretized as proposed

by Trias et al. [32] in order to ensure that the resulting diffusive operator is symmetric and positive-definite. The notation and geometrical parameters are graphically illustrated in Fig. 1.

Next, dividing Eq. 10 by density, ρ^{n+1}, multiplying by the divergence operator, applying the incompressibility condition, Eq. 1, and discretizing over a cell c, yields the discrete Poisson's pressure equation of the form

$$\sum_{f \in F(c)} \frac{\hat{M}_f^p}{\rho_f^{n+1}} = \Delta t \sum_{f \in F(c)} \frac{1}{\rho_f^{n+1}} (p_{nb}^{n+1} - p_c^{n+1}) \frac{A_f}{\delta d_f}, \tag{13}$$

which solves the pressure field at time instant $n+1$. Following the obtention of this p^{n+1} field, $\mathbf{u}^{n+1}$ results from discretizing Eq. 10 over a cell c as

$$\mathbf{u}_c^{n+1} = \mathbf{u}_c^p - \frac{\Delta t}{\rho_c^{n+1} V_c} \sum_{f \in F(c)} p_f^{n+1} \hat{\mathbf{n}}_f A_f, \tag{14}$$

where p_f is the pressure interpolated to face f.

Notice that expressions for $\boldsymbol{\phi}_f^n$, ρ_f^{n+1}, $\mathbf{u}_f^p$, $\hat{M}_f^p$, and p_f^{n+1} have not been specified yet. As introduced before and studied in Sec. 3, quantitites evaluated at cell faces need specific interpolations in order to minimize the kinetic energy conservation error. In this regard, the low-dissipation convection scheme proposed is detailed and analyzed in Sec. 4. Following this idea, density, predictor velocity, pressure, and mass flux at face f are calculated

as

$$\rho_f^{n+1} = \frac{1}{2}(\rho_c^{n+1} + \rho_{nb}^{n+1}), \quad \mathbf{u}_f^p = \frac{1}{2}(\mathbf{u}_c^p + \mathbf{u}_{nb}^p), \quad p_f^{n+1} = \frac{1}{2}(p_c^{n+1} + p_{nb}^{n+1}), \tag{15}$$

$$\hat{M}_f^p = \rho_f^{n+1}\mathbf{u}_f^p \cdot \hat{\mathbf{n}}_f A_f. \tag{16}$$

Finally, evaluation of the mass flux at face f, $\hat{M}_f^{n+1}$, needs to be studied in detail in order to exactly conserve mass. Thus, taking again the divergence of Eq. 10 and discretizing over a cell c, gives

$$\sum_{f \in F(c)} \hat{M}_f^{n+1} - \sum_{f \in F(c)} \hat{M}_f^p = -\Delta t \sum_{f \in F(c)} (p_{nb}^{n+1} - p_c^{n+1}) \frac{A_f}{\delta d_f}, \tag{17}$$

which may be rearranged in the following form

$$\sum_{f \in F(c)} \left[\hat{M}_f^{n+1} - \hat{M}_f^p + \Delta t (p_{nb}^{n+1} - p_c^{n+1}) \frac{A_f}{\delta d_f} \right] = 0. \tag{18}$$

Different possibilities exist to solve this underdetermined system of equations. For example, the strategy chosen in this work is to set to zero each face summand —it is a more restrictive condition, but at the same time provides an easier formulation. Then, the mass flux at face f is expressed as

$$\hat{M}_f^{n+1} = \hat{M}_f^p - \Delta t (p_{nb}^{n+1} - p_c^{n+1}) \frac{A_f}{\delta d_f}. \tag{19}$$

At this point, if the predictor mass flux is evaluated by means of Eq. 16 and

$\mathbf{u}^p$ is substituted using Eq. 14, Eq. 19 may be rewritten (similarly as [3]) as

$$\hat{M}_f^{n+1} = \rho_f^{n+1}\frac{1}{2}(\mathbf{u}_c^{n+1} + \mathbf{u}_{nb}^{n+1})\cdot\hat{\mathbf{n}}_f A_f - \Delta t(p_{nb}^{n+1} - p_c^{n+1})\frac{A_f}{\delta d_f} \tag{20}$$
$$+ \frac{\rho_f^{n+1}\Delta t}{2}\left[\frac{1}{\rho_c^{n+1}V_c}\sum_{f\in F(c)} p_f^{n+1}\hat{\mathbf{n}}_f A_f + \frac{1}{\rho_{nb}^{n+1}V_{nb}}\sum_{f\in F(nb)} p_f^{n+1}\hat{\mathbf{n}}_f A_f\right]\cdot\hat{\mathbf{n}}_f A_f.$$

Regardless of the interface-capturing method adopted, the mass flux resulting from Eq. 20 is used to advect the phase volume fractions, C_k, through the transport equation, Eq. 6. Details of the interface-capturing methods used in this work can be found in [8, 9] and [3] for the VOF and LS approaches, respectively.

3. Conservation properties

The continuity and Navier-Stokes equations are derived specifically for the conservation of mass and momentum. Thus, finite-volume based discretizations inherently preserve these properties. On the contrary, conservation of secondary derived quantities, such as kinetic energy, entropy or vorticity — which cannot be directly imposed during the construction of the numerical methods — is not always considered.

In this section, discrete conservation properties of the collocated scheme for two-phase flow without surface tension (introduced in Jofre et al. [33]) are theoretically analyzed. Discussion of kinetic energy preservation, partitioned between this section and Sec. 4, is presented for a generic treatment of the

convective operator. For this purpose, it is useful to introduce the matrix-vector notation of the governing equations, Eqs. 1 and 2, written as

$$\mathbf{M}\mathbf{u} = \mathbf{0}, \tag{21}$$

$$\mathbf{\Omega}\frac{d(\rho\mathbf{u})}{dt} + \mathbf{C}(\rho\mathbf{u})\mathbf{u} + \mathbf{G}\mathbf{p} + \mathbf{D}(\mu)\mathbf{u} + \mathbf{\Omega}\mathbf{S} = \mathbf{0}, \tag{22}$$

where $\mathbf{u}$, $\mathbf{p}$ and $\mathbf{S}$ are the vectors of velocities, pressures and source terms. The diagonal matrix $\mathbf{\Omega}$ describes the volume of cells, matrices $\mathbf{C}(\rho\mathbf{u})$ and $\mathbf{D}(\mu)$ are the convective and diffusive operators, and matrices $\mathbf{G}$ and $\mathbf{M}$ represent the gradient and divergence operators, respectively.

As proposed by Verstappen and Veldman [26], discrete conservation properties are easily analyzed by considering the symmetries of these matrices. On the one hand, kinetic energy is conserved if and only if the discrete convective operator is skew-symmetric, i.e., the transpose of the matrix is also its negative, $\mathbf{C}(\rho\mathbf{u}) = -\mathbf{C}(\rho\mathbf{u})^*$, and if the negative conjugate transpose of the discrete gradient operator is equal to the divergence operator, i.e., $\mathbf{M} = -\mathbf{G}^*$. On the other hand, the diffusive operator must be symmetric and positive-definite in order to be dissipative, i.e., the matrix is equal to its transpose $\mathbf{D}(\mu) = \mathbf{D}(\mu)^*$, and $\mathbf{z}^*\mathbf{D}(\mu)\mathbf{z} > \mathbf{0}$ for all nonzero vector $\mathbf{z}$.

3.1. Mass conservation

Global mass conservation invokes the integral of Eq. 1 over the whole domain, Ω. Thus, if the entire integral is transformed to a summation of integrals for each control volume that form the domain, $c \in \Omega$, the following

expression is obtained

$$\int_{\Omega} \nabla\cdot\mathbf{u}\; dV = \sum_{c\in\Omega}\int_{\Omega_c} \nabla\cdot\mathbf{u}\; dV = \sum_{c\in\Omega}\sum_{f\in F(c)} \hat{U}_f A_f. \tag{23}$$

Defining the normal face velocity U_f, as the mass flux at a face M_f, divided by face density ρ_f, and area A_f, rewrites Eq. 23 as

$$\int_{\Omega} \nabla\cdot\mathbf{u}\; dV = \sum_{c\in\Omega}\sum_{f\in F(c)} \hat{U}_f A_f = \sum_{c\in\Omega}\sum_{f\in F(c)} \frac{\hat{M}_f}{\rho_f}. \tag{24}$$

For the collocated scheme, a special definition for mass fluxes at faces, Eq. 20, has been developed in order to exactly conserve mass on each cell c. Thus, the local conservation of mass for the collocated scheme is demonstrated by dividing Eq. 17 by face density, rearranging terms and making use of Eq. 13, giving

$$\sum_{f\in F(c)} \frac{\hat{M}_f^{n+1}}{\rho_f^{n+1}} = \sum_{f\in F(c)} \left[\frac{\hat{M}_f^{p}}{\rho_f^{n+1}} - \frac{\Delta t}{\rho_f^{n+1}} (p_{nb}^{n+1} - p_c^{n+1}) \frac{A_f}{\delta d_f} \right] = 0. \tag{25}$$

Therefore, total mass preservation results directly from local conservation at each cell, which is expressed as

$$\int_{\Omega} \nabla\cdot\mathbf{u}\; dV = \sum_{c\in\Omega}\int_{\Omega_c} \nabla\cdot\mathbf{u}\; dV = \sum_{c\in\Omega}\sum_{f\in F(c)} \hat{U}_f A_f = \sum_{c\in\Omega}\sum_{f\in F(c)} \frac{\hat{M}_f}{\rho_f} = 0. \tag{26}$$

3.2. Momentum conservation

Conservation of momentum is intrinsically guaranteed by writing the equations in divergence form. It is obtained by integrating Eq. 2 over the entire domain, which is transformed to a summation of integrals for each control volume that form the domain and converted to surface integrals by applying the divergence theorem, resulting in

$$\sum_{c\in\Omega}\frac{d(\rho_c\mathbf{u}_c)}{dt}V_c+\sum_{c\in\Omega}\sum_{f\in F(c)}\boldsymbol{\phi}_f\hat{M}_f=-\sum_{c\in\Omega}\sum_{f\in F(c)}p_f\hat{\mathbf{n}}_fA_f \qquad (27)$$
$$+\sum_{c\in\Omega}\sum_{f\in F(c)}\mu_f\left[(\mathbf{u}_{nb}-\mathbf{u}_c)\frac{A_f}{\delta d_f}+\nabla^{\intercal}\mathbf{u}_f\cdot\hat{\mathbf{n}}_fA_f\right]+\sum_{c\in\Omega}\mathbf{S}_cV_c.$$

Notice that $\hat{M}_f$, $\hat{\mathbf{n}}_f$ and $(\mathbf{u}_{nb}-\mathbf{u}_c)$ are quantities that present equal values but with different sign when evaluating them at a face f from two adjacent interior cells. In this way, interior fluxes cancel out and Eq. 27 is evaluated as the summation over boundary faces $f\in F(\partial\Omega)$ written as

$$\sum_{c\in\Omega}\frac{d(\rho_c\mathbf{u}_c)}{dt}V_c+\sum_{f\in F(\partial\Omega)}\boldsymbol{\phi}_f\hat{M}_f=-\sum_{f\in F(\partial\Omega)}p_f\hat{\mathbf{n}}_fA_f \qquad (28)$$
$$+\sum_{f\in F(\partial\Omega)}\mu_f\left[(\mathbf{u}_f-\mathbf{u}_a)\frac{A_f}{\delta d_f}+\nabla^{\intercal}\mathbf{u}_f\cdot\hat{\mathbf{n}}_fA_f\right]+\sum_{c\in\Omega}\mathbf{S}_cV_c,$$

where $\mathbf{u}_a$ is the boundary-neighbor cell velocity. This equation states that the change in momentum is due to the fluxes through the boundary of the domain and the source terms.

3.3. Kinetic energy conservation

The transport equation for kinetic energy, $\frac{1}{2}\rho\mathbf{u}\cdot\mathbf{u}$, is derived from the momentum equation, Eq. 2, by taking the velocity dot product and assuming incompressible fluid. Its mathematical expression takes the form

$$\frac{\partial(\frac{1}{2}\rho\mathbf{u}\cdot\mathbf{u})}{\partial t}+\nabla\cdot\left[\mathbf{u}(\frac{1}{2}\rho\mathbf{u}\cdot\mathbf{u})\right]=-\nabla\cdot(p\mathbf{u}) \\ +\nabla\cdot[\mu(\nabla\mathbf{u}+\nabla^{\intercal}\mathbf{u})]\cdot\mathbf{u}+\mathbf{S}\cdot\mathbf{u}, \tag{29}$$

where, from left to right, quantities correspond to time derivative, convection, pressure, diffusion and source terms, respectively. In order to investigate the conservation of kinetic energy for the collocated scheme, Eq. 29 is discretized over the whole domain and transformed to a summation of surface integrals for each cell c as

$$\sum_{c\in\Omega}\mathbf{u}_c\cdot\frac{d(\rho_c\mathbf{u}_c)}{dt}V_c+\sum_{c\in\Omega}\mathbf{u}_c\cdot\sum_{f\in F(c)}\boldsymbol{\phi}_f\hat{M}_f=-\sum_{c\in\Omega}\mathbf{u}_c\cdot\sum_{f\in F(c)}p_f\hat{\mathbf{n}}_fA_f \\ +\sum_{c\in\Omega}\mathbf{u}_c\cdot\sum_{f\in F(c)}\mu_f\left[(\mathbf{u}_{nb}-\mathbf{u}_c)\frac{A_f}{\delta d_f}+\nabla^{\intercal}\mathbf{u}_f\cdot\hat{\mathbf{n}}_fA_f\right]+\sum_{c\in\Omega}\mathbf{u}_c\cdot\mathbf{S}_cV_c. \tag{30}$$

The detailed analysis of the pressure term in Eq. 30 is simplified by introducing an identity involving combinations of interpolation and differentiation operators. The relation, first presented by Morinishi et al. [34] and restated

in finite-volume form by Felten and Lund [35], reads

$$\varphi_c \sum_{f\in F(c)} \bar{\psi}_f Q_f + \psi_c \sum_{f\in F(c)} \bar{\varphi}_f Q_f = \sum_{f\in F(c)} \widehat{\varphi\psi} Q_f + (\varphi_c\psi_c) \sum_{f\in F(c)} Q_f, \tag{31}$$

where φ and ψ are two general variables, Q_f is a general quantity known on the cell face, i.e., no interpolation is needed, the overbars refer to interpolated values, and $\widehat{\varphi\psi} = \frac{1}{2}(\varphi_c\psi_{nb} + \varphi_{nb}\psi_c)$ is a special interpolator operator for products.

Specifying the above identity to the pressure term by taking $\varphi = \mathbf{u}$, $\psi = p$ and $Q_f = \hat{\mathbf{n}}_f A_f$, and using Eq. 20 to simplify the expression, results in the following relation

$$\begin{aligned}\sum_{c\in\Omega} \mathbf{u}_c \cdot \sum_{f\in F(c)} p_f \hat{\mathbf{n}}_f A_f = \sum_{c\in\Omega} \sum_{f\in F(c)} \widehat{\mathbf{u}p} \cdot \hat{\mathbf{n}}_f A_f - \sum_{c\in\Omega} p_c \sum_{f\in F(c)} \frac{\Delta t}{\rho_f} \left[(p_{nb} - p_c) \frac{A_f}{\delta d_f} \right] \\ + \sum_{c\in\Omega} p_c \sum_{f\in F(c)} \frac{\Delta t}{2} \left[\frac{1}{\rho_c V_c} \sum_{f\in F(c)} p_f \hat{\mathbf{n}}_f A_f + \frac{1}{\rho_{nb} V_{nb}} \sum_{f\in F(nb)} p_f \hat{\mathbf{n}}_f A_f \right] \cdot \hat{\mathbf{n}}_f A_f.\end{aligned} \tag{32}$$

Finally, noticing that interior fluxes in Eq. 32 cancel out, Eq. 30 can be

rewritten as

$$\sum_{c\in\Omega}\frac{d(\frac{1}{2}\rho_c\mathbf{u}_c\cdot\mathbf{u}_c)}{dt}V_c+\sum_{c\in\Omega}\mathbf{u}_c\cdot\sum_{f\in F(c)}\boldsymbol{\phi}_f\hat{M}_f= \tag{33}$$
$$-\sum_{f\in F(\partial\Omega)}\frac{1}{2}\left(\mathbf{u}_a p_f+\mathbf{u}_f p_a\right)\cdot\hat{\mathbf{n}}_f A_f+\sum_{c\in\Omega}p_c\sum_{f\in F(c)}\frac{\Delta t}{\rho_f}\left[(p_{nb}-p_c)\frac{A_f}{\delta d_f}\right]$$
$$-\sum_{c\in\Omega}p_c\sum_{f\in F(c)}\frac{\Delta t}{2}\left[\frac{1}{\rho_c V_c}\sum_{f\in F(c)}p_f\hat{\mathbf{n}}_f A_f+\frac{1}{\rho_{nb}V_{nb}}\sum_{f\in F(nb)}p_f\hat{\mathbf{n}}_f A_f\right]\cdot\hat{\mathbf{n}}_f A_f$$
$$+\sum_{c\in\Omega}\mathbf{u}_c\cdot\sum_{f\in F(c)}\mu_f\left[(\mathbf{u}_{nb}-\mathbf{u}_c)\frac{A_f}{\delta d_f}+\nabla^{\intercal}\mathbf{u}_f\cdot\hat{\mathbf{n}}_f A_f\right]+\sum_{c\in\Omega}\mathbf{u}_c\cdot\mathbf{S}_c V_c,$$

which states that in the absence of viscosity ($\mu = 0$) and source terms, the change in kinetic energy is due to the fluxes through the boundary of the domain plus a kinetic energy error related to the pressure term. This error is intrinsic to the collocated formulation, and results from the different pressure gradient evaluations in Eqs. 14 and 17 necessary to evaluate velocities at centers of cells and mass fluxes at time $n+1$, respectively. This result is related to the symmetries of discrete operators by noticing that the different pressure gradient evaluations do not respect the relation $\mathbf{M} = -\mathbf{G}^*$. Moreover, as further discussed in Sec. 4, an additional error appears if the convection scheme $\boldsymbol{\phi}_f$ is not skew-symmetric.

In order to complete the analysis, it is important to evaluate the scaling order of the kinetic energy pressure error, since it can not be eliminated. In this regard, the error is easily analyzed when simplifying it for each individual

face f as

$$\Delta t A_f \left[\frac{(p_{nb} - p_c)}{\rho_f \delta d_f} - \frac{1}{2} \left(\sum_{f \in F(c)} \frac{p_f \hat{\mathbf{n}}_f A_f}{\rho_c V_c} + \sum_{f \in F(nb)} \frac{p_f \hat{\mathbf{n}}_f A_f}{\rho_{nb} V_{nb}} \right) \cdot \hat{\mathbf{n}}_f \right], \quad (34)$$

showing that the total term depends on the density ratio between the two cells adjacent to the face, ρ_c/ρ_{nb}, and is multiplied by time step Δt, and face surface A_f. Hence, the pressure error is proportional to $\Delta\rho$, while spatially scaled as $\mathcal{O}(\Delta h^2)$ and temporally scaled as $\mathcal{O}(\Delta t)$, although it can be reduced through the use of different temporal integration schemes, $\mathcal{O}(\Delta t^m)$, as proposed by Felten and Lund [35] and studied by Fishpool and Leschziner [36].

4. Low-dissipation convection scheme

The finite-volume discretization of the convective operator is carried out by isolating the convection term in Eq. 2 and integrating it over the volume of a cell c, Ω_c. Next, divergence theorem is applied to the bordering faces of the cell $f \in F(c)$, and the expression is reduced by identifying the part corresponding to the mass flux as

$$\int_{\Omega_c} \nabla \cdot (\rho \mathbf{u}\mathbf{u})\, dV = \sum_{f \in F(c)} \rho_f \mathbf{u}_f \boldsymbol{\phi}_f \cdot \hat{\mathbf{n}}_f A_f = \sum_{f \in F(c)} \boldsymbol{\phi}_f \hat{M}_f, \quad (35)$$

where $\hat{\mathbf{n}}_f$, A_f and $\hat{M}_f$ are the normal outward unit vector, the surface and the mass flow corresponding to face f, respectively, whereas $\boldsymbol{\phi}_f$ is the value of $\mathbf{u}$ at face f evaluated by a convective numerical scheme. A graphical

representation of these parameters is shown in Fig. 1.

Many different strategies are available in the literature for the evaluation of $\boldsymbol{\phi}_f$. Among them, the symmetry-preserving scheme presents discrete conservation of kinetic energy, although it may result unstable in variable-density regions. Alternatively, the upwind scheme improves numerical stability, however, at expenses of adding artificial dissipation into the discrete system. The solution proposed in this work consists in the hybridization of these two approaches to construct a low-dissipation and low-dispersion convection scheme suitable for turbulent interfacial flow.

In this section, the description of the hybrid convection scheme is detailed in three steps. First, the symmetry-preserving and upwind schemes are presented. Second, the hybridization process is formulated. Finally, the discrete kinetic energy conservation properties of the scheme are theoretically analyzed.

4.1. Symmetry-preserving

The symmetry-preserving scheme [26] discretizes the convection term by means of a skew-symmetric discrete operator; i.e., the discrete convective operator satisfies $\mathbf{C}(\rho\mathbf{u}) = -\mathbf{C}(\rho\mathbf{u})^*$. This particular construction of the convective operator ensures that no artificial dissipation is introduced into the discrete system of equations by the convection term. This property is fundamental if turbulence dominates the physics of the problems under consideration. Indeed, in the absence of source terms, kinetic energy should

only be dissipated by viscous forces. Therefore, discretization strategies with excessive numerical dissipation can significantly alter the physics of the flow.

In order to construct a discrete skew-symmetric convective operator, $\boldsymbol{\phi}_f$ must be evaluated as

$$\boldsymbol{\phi}_f = \frac{\boldsymbol{\phi}_P + \boldsymbol{\phi}_F}{2}, \tag{36}$$

where $\boldsymbol{\phi}_P$ and $\boldsymbol{\phi}_F$ correspond to the values of $\mathbf{u}$ at the neighboring cells of face f; see Fig. 1. As demonstrated in Sec. 5.2, this convection scheme is first-order accurate on 3-D unstructured meshes, while it increases its accuracy to second-order on Cartesian grids. Higher-order versions of this scheme are available [26]. However, for the ease of exposition, the hybrid scheme will be presented in terms of the first-order version.

4.2. Upwind

The upwind scheme [30] approximates the convection term by a diagonally-dominant positive real discrete operator; i.e., the entries in the i'th row and j'th column, c_{ij}, of matrix $\mathbf{C}(\rho\mathbf{u})$ are $|c_{ii}| \geq \sum_{j\neq i}|c_{ij}|$ for all i, and $\mathbf{z}^\intercal\mathbf{C}(\rho\mathbf{u})\mathbf{z} > \mathbf{0}$ for all nonzero real vector $\mathbf{z}$. This type of convective operator has a slowing-down effect on the discrete flow solutions by adding artificial dissipation, irrespective of grid irregularity, into the problems. This property is not desirable for the correct resolution of turbulence, but may be of key importance to mitigate the growth of spurious currents near interfaces, and therefore stabilize the calculation.

In particular, the upwind scheme considered is constructed by adding a

dissipative term into the previous symmetry-preserving expression. This is mathematically formulated as

$$\boldsymbol{\phi}_f = \frac{\boldsymbol{\phi}_P + \boldsymbol{\phi}_F}{2} - \frac{|\hat{M}_f|}{\hat{M}_f}\frac{\boldsymbol{\phi}_F - \boldsymbol{\phi}_P}{2}, \tag{37}$$

where $\hat{M}_f$ is the outward-oriented mass flow at face f; see Fig. 1. The accuracy of this upwind scheme is also first-order on 3-D unstructured meshes and second-order on Cartesian grids.

4.3. Hybridization

The final step is the formulation of the schemes hybridization. Briefly, $\boldsymbol{\phi}_f$ is evaluated according to the symmetry-preserving scheme, Eq. 36, for all the faces of the mesh, except for those adjoining at least one cell containing an interface, where the stabilizing scheme, Eq. 37, is activated. This hybrid operator can be expressed in a single equation as

$$\boldsymbol{\phi}_f = \frac{\boldsymbol{\phi}_P + \boldsymbol{\phi}_F}{2} - \alpha_f\frac{|\hat{M}_f|}{\hat{M}_f}\frac{\boldsymbol{\phi}_F - \boldsymbol{\phi}_P}{2}, \tag{38}$$

where α_f is a coefficient that takes value 1 for the set of faces belonging at least to one cell containing an interface, and takes value 0 otherwise; see Fig. 2.

At this point is where the interface-capturing method is utilized since it is a natural interface sensor. Remember that Eq. 6 locates the transient position of the interface by means of scalar values corresponding to the phase

k volume fraction within each cell. Therefore, the C_k scalar field itself can be directly used to identify the faces that belong to cells containing an interface. In a mathematical form, this is expressed as

$$\alpha_{f\in F(c)} = \begin{cases} 1 & \text{if } 0 < C_k[c,t] < 1, \\ 0 & \text{otherwise,} \end{cases} \tag{39}$$

where $\alpha_{f\in F(c)}$ corresponds to the values of α_f for the faces of cell c, and $C_k[c,t]$ is the volume-fraction value of phase k within cell c at time instant t. Depending on the interface-capturing method chosen, the hybridization will be activated on a smaller or larger band. For instance, if using the VOF method, only the faces of the cells containing an interface will assume $\alpha_f = 1$, as in the example shown in Fig. 2. Differently, when using the LS method, the hybridized region will be wider, coinciding with the variable-density zone around Γ with thickness controlled by parameter ε in Eq. 9.

4.4. Convective kinetic energy conservation

The diagonal elements of the discrete convective matrix, $\mathbf{C}(\rho\mathbf{u})$ of dimension $m \times m$, corresponding to the hybrid symmetry-preserving upwind scheme are

$$c_{ii} = \sum_{f\in F(i)} \frac{1}{2}\left(\hat{M}_f + \alpha_f|\hat{M}_f|\right) \qquad \forall i = 1, ..., m, \tag{40}$$

whereas the off-diagonal elements equal

$$c_{ij} = \frac{1}{2}\left(\hat{M}_{ij} - \alpha_{ij}|\hat{M}_{ij}|\right), \tag{41}$$

in the case of existing face-connectivity between cells i and j, while are null otherwise. The distribution of the matrix $\mathbf{C}(\rho\mathbf{u})$ eigenvalues on the real-imaginary plot is based on the following proposition.

Proposition 1. *The eigenvalues of a symmetric positive matrix (with real entries) are positive real, and the eigenvalues of a skew-symmetric matrix are pure imaginary.*

As exemplified in Fig. 3, three different situations may be encountered, corresponding to the cells labeled as **a**, **b** and **c** in Fig. 2. First, in the case of a cell i located far from an interface, e.g., cell **a**, α_f equals 0 for all its faces and ρ is constant. Consequently, the following result is obtained from the finite-volume discretization of the continuity equation on the cell

$$\int_{\Omega_i} \nabla\cdot\mathbf{u}\, dV = \sum_{f\in F(i)} \mathbf{u}_f\cdot\hat{\mathbf{n}}_f A_f = \frac{1}{\rho}\sum_{f\in F(i)} \rho\mathbf{u}_f\cdot\hat{\mathbf{n}}_f A_f = \frac{1}{\rho}\sum_{f\in F(i)} \hat{M}_f = 0. \tag{42}$$

Therefore, Eqs. 40 and 41 reduce to

$$c_{ii} = 0 \quad \text{and} \quad c_{ij} = \frac{1}{2}\hat{M}_{ij}. \tag{43}$$

The resulting submatrix is skew-symmetric, in consequence, it follows from

Prop. 1 that its eigenvalue lies on the imaginary axis: $\lambda_i^C \in \mathbb{I}$. Second, considering the case of a cell i containing an interface, e.g., cell **b**, it is straightforward from Fig. 2 that α_f is 1 for all its faces, and consequently Eqs. 40 and 41 are rewritten as

$$c_{ii} = \sum_{f \in F(i)} \frac{1}{2}\left(\hat{M}_f + |\hat{M}_f|\right) \quad \text{and} \quad c_{ij} = \frac{1}{2}\left(\hat{M}_{ij} - |\hat{M}_{ij}|\right), \tag{44}$$

which is a diagonally-dominant positive submatrix. Thus, under the hypothesis of Prop. 1, the eigenvalue of the submatrix is positive real: $\lambda_i^C \in \mathbb{R}^+$. Third, in a situation where the faces of a cell i take different values of α_f, e.g., cell **c**, it is direct from the two previous cases that the eigenvalue of the corresponding submatrix lives on the positive real part of the complex numbers: $\lambda_i^C \in \mathbb{C} \mid \Re(\lambda_i^C) \in \mathbb{R}^+$.

The location of the eigenvalues on the real-imaginary diagram has direct relation with the discrete conservation of kinetic energy. In particular, the transport equation for kinetic energy, $\frac{1}{2}\rho\mathbf{u}\cdot\mathbf{u}$, is derived from the momentum equation, Eq. 2, by taking the velocity dot product. Hence, multiplying the convection term, expressed in discrete matrix operators, by the velocity vector $\mathbf{u}$ and taking into account the definition of eigenvalue, i.e., $\mathbf{C}(\rho\mathbf{u})\mathbf{u} = \lambda^C\mathbf{u}$, results in

$$[\mathbf{C}(\rho\mathbf{u})\mathbf{u}] \cdot \mathbf{u} = \left[\lambda_i^C \mathbf{u}_i\right] \cdot \mathbf{u}_i \qquad \forall i = 1, ..., m. \tag{45}$$

Then, depending on the value taken by λ_i^C, the vector $\lambda_i^C \mathbf{u}_i$ is: (1) if $\lambda_i^C \in \mathbb{I}$, just a rotation of vector $\mathbf{u}_i$ around its axis; (2) if $\lambda_i^C \in \mathbb{R}^+$, a deformation of vector $\mathbf{u}_i$ without direction change; or (3) if $\lambda_i^C \in \mathbb{C} \mid \Re(\lambda_i^C) \in \mathbb{R}^+$, a combination of the two previous cases. Consequently, the variation of kinetic energy due to the convection term, written as

$$\mathbf{u}_i \cdot \mathbf{u}_i - \left[\lambda_i^C \mathbf{u}_i\right] \cdot \mathbf{u}_i, \tag{46}$$

is zero for case (1), nonzero for case (2) and between zero and a nonzero value for case (3). Therefore, there is no dissipation of kinetic energy by the convection term if an eigenvalue lies on the imaginary axis, while, if it lives on the positive real part of the complex numbers and $\lambda_i^C < 1$, the convection term adds dissipation into the discrete system and, more important, is of positive sign, i.e., acts as a kinetic energy reliever. In conclusion, the use of the hybrid scheme confines kinetic energy dissipation to the subgroup of cells close to the interfaces. It is worth stressing that this dissipation depends on the interface-capturing method chosen. For instance, given the wider extension of the interface region, the LS method presents larger dissipation than the VOF approach.

5. Numerical tests

Four different tests are considered for analyzing the properties of the low-dissipation and low-dispersion method proposed. First, kinetic energy

conservation properties are assessed by numerically resolving the evolution of a 3-D vortex. Second, an accuracy assessment is presented using an exact sinusoidal function. Next, the scheme is tested for cases in which the interface-capturing method is coupled to the equations of fluid motion. Initially, a spherical drop first in equilibrium and later submerged in a swirling velocity field is considered as a case to test the capacity of the model to diminish spurious velocities. Finally, its robustness and accuracy are demonstrated by numerically calculating a two-phase turbulent coaxial jet.

The results reported in this work have been performed with the *TermoFluids* Computational Fluid Dynamics (CFD) software package [37], in which the hybrid symmetry-preserving upwind scheme has been integrated into an existing multiphase library.

5.1. Three-dimensional vortex

The conservation of kinetic energy related to the convection term is analyzed numerically by solving a 3-D vortex with zero net mass flux at the boundaries and no interface advection. The set of 3-D vortices shown in Fig. 4 are initially described by

$$\begin{aligned} u &= A cos(kx) sin(ky) sin(kz), \\ v &= -A sin(kx) cos(ky) sin(kz), \\ w &= 0, \end{aligned} \tag{47}$$

where $A = 1.0 \times 10^{-3}\ m/s$ is the velocity amplitude and $k = 1$ is the wave number. The vortex is solved in a box of side $2\pi \times 2\pi \times 2\pi$ meshed by means of 6.6×10^4 triangular prisms that correspond to a mesh size of $h = 0.2$. In detail, the 3-D mesh is generated by extruding a 2-D grid —composed of 2.2×10^3 triangles— 30 times with a constant length step. The box is filled with two different fluids. One with density $\rho_1 = 1\ kg/m^3$ occupying the entire cube except for a sphere of diameter $D = \pi$ located in the center of the box. This sphere is filled with a different fluid of density ρ_2. In order to study the properties of the different convection schemes, four different cases are analyzed in which progressively larger density ratios between inner and outer fluids, $\mathbf{r}_\rho = \rho_2/\rho_1$, are considered. In particular, ρ_2 is set to 1, 10, 100 and 1000 kg/m^3. A constant time step of $\Delta t = 1.0 \times 10^{-3}\ s$ is used, and slip-wall conditions are applied to all boundaries.

In the absence of body and interfacial forces, and considering incompressible inviscid flow, i.e., $\nabla \cdot \mathbf{u} = 0$ and $\mu = 0$, the kinetic energy conservation equation, Eq. 29, reduces to

$$\frac{\partial(\frac{1}{2}\rho\mathbf{u}\cdot\mathbf{u})}{\partial t} + \nabla \cdot \left[\mathbf{u}(\frac{1}{2}\rho\mathbf{u}\cdot\mathbf{u})\right] = -\nabla\cdot(p\mathbf{u}). \tag{48}$$

It is important to note that this equation is intrinsically conservative, as kinetic energy is just redistributed, not created neither dissipated. Therefore, the rate of change of kinetic energy by the convection term is zero. Similarly, discrete systems will be kinetic energy conservative if the convective and

pressure operators are shown to be conservative.

Focusing on the convection term, the test proposed here is appropriate to study its kinetic energy conservation since there is no net mass flux across boundaries. This enables a proper characterization, in terms of rate of change of kinetic energy, of the symmetry-preserving (*sp*), upwind (*uw*) and hybrid symmetry-preserving upwind (*hspu*) convection schemes. In this regard, the norm of the kinetic energy rate of change by the convection term, $|\nabla \cdot \mathbf{u}(\frac{1}{2}\rho\mathbf{u} \cdot \mathbf{u})|$, is calculated at every time step by integrating the convection term in Eq. 48 over the entire domain, Ω, transforming it to a summation of integrals for each control volume that form the domain $c \in \Omega$, and using the divergence theorem to simplify the expression as

$$\int_{\Omega} \nabla \cdot \mathbf{u}(\frac{1}{2}\rho\mathbf{u} \cdot \mathbf{u})\, dV = \frac{1}{2}\sum_{c\in\Omega} \mathbf{u}_c \cdot \sum_{f\in F(c)} \boldsymbol{\phi}_f \hat{M}_f. \tag{49}$$

Results are reported in Tab. 1 for each scheme, and for increasing values of density ratio between fluids. In all cases, the total rate of change of kinetic energy, $\partial(\frac{1}{2}\rho\mathbf{u} \cdot \mathbf{u})/\partial t$, is determined mainly by the convection term with the pressure contribution, $|\nabla \cdot (p\mathbf{u})|$, negligible. The case of uniform density between fluids shows that the *sp* scheme produces zero variation of kinetic energy. On the contrary, the *uw* scheme introduces dissipation of value $\mathcal{O}(10^{-8})$ into the discrete system, while *hspu* consistently reduces the dissipation to $\mathcal{O}(10^{-9})$ by restricting the stabilization to the interface region. Similar trends are observed when assigning different densities to the fluids.

In the case of $\mathbf{r}_\rho = 10$, *sp* results in zero variation (machine precision) of kinetic energy. Conversely, the dissipation introduced is of order $\mathcal{O}(10^{-7})$ for *uw* and $\mathcal{O}(10^{-8})$ for *hspu*, and increases with larger density differences. It is important to notice that, despite its small magnitude, the errors in *sp* slightly increase with the density ratio due to the difficulty of the Poisson solver to reach machine precision.

Results in Tab. 1 account for the accumulated variation of kinetic energy by the convection term over the entire domain. However, it is interesting to analyze the particular value for each individual cell. The convection term of the kinetic energy transport equation, Eq. 29, can be written in discrete matrix-vector notation by left-multiplying $\mathbf{C}(\rho\mathbf{u})$ by $\mathbf{u}^*$ and summing the resulting expression with its conjugate transpose, resulting in

$$\mathbf{u}^* \left[\mathbf{C}(\rho\mathbf{u}) + \mathbf{C}^*(\rho\mathbf{u})\right] \mathbf{u}. \tag{50}$$

Next, considering the general expression of the *hspu* convection scheme given by Eqs. 40 and 41, and accounting for the contribution of each cell c — diagonal elements of the $\mathbf{C}(\rho\mathbf{u}) + \mathbf{C}^*(\rho\mathbf{u})$ matrix— , the above equation can be reduced to

$$\mathbf{u}_c \cdot \sum_{f \in F(c)} \left(\hat{M}_f + \alpha_f |\hat{M}_f|\right) \mathbf{u}_c. \tag{51}$$

Notice that if α_f is 0 the expression collapses to the *sp* convection scheme, whereas $\alpha_f = 1$ corresponds to the *uw* case.

The mathematical expression introduced is evaluated for the three schemes,

and the results are presented in terms of relative error with respect to the values obtained with *sp* as

$$\varepsilon_{\text{conv},x} = \frac{|\left[\partial(\frac{1}{2}\rho\mathbf{u}\cdot\mathbf{u})/\partial t\right]_x - \left[\partial(\frac{1}{2}\rho\mathbf{u}\cdot\mathbf{u})/\partial t\right]_{sp}|}{|\left[\partial(\frac{1}{2}\rho\mathbf{u}\cdot\mathbf{u})/\partial t\right]_{sp}|}, \tag{52}$$

with x representing the *uw* or *hspu* convection schemes. Results for $\mathbf{r}_\rho = 100$ are plotted in Fig. 5 for the cells laying along a radial direction of the sphere with dimensionless coordinate $\hat{r} = r/R$. The figure corroborate that the *uw* scheme dissipates kinetic energy for all cells with a peak in the variable density region, whereas the *hspu* scheme is conservative, i.e., $\varepsilon_{\text{conv},hspu} = 0$, except for the cells close to the interface ($\hat{r} = 1$) where α_f is activated to 1, and therefore the *uw*-dissipation is introduced. In this region, $\varepsilon_{\text{conv},hspu}$ tends to the $\varepsilon_{\text{conv},uw}$ value.

5.2. Exact sinusoidal function

The spatial accuracy of the hybrid symmetry-preserving upwind (*hspu*) scheme, together with the ones of the symmetry-preserving (*sp*) and upwind (*uw*) schemes, is studied by means of comparing numerical results to the analytical solution of an exact sinusoidal function. On the one hand, for each convection scheme, the numerical values of the convection term on each cell are calculated from the right-hand side of Eq. 35, with the corresponding $\boldsymbol{\phi}_f$ definition, Eqs. 36-38, by assigning a sinusoidal function to the input variables: (1) velocities at centers of cells $\mathbf{u}_c$, and (2) face mass fluxes at faces $\hat{M}_f$. On the other hand, analytical values are obtained by directly

evaluating the left-hand side of Eq. 35. Finally, analytical and numerical results are compared by means of the root-square-mean error (rms) x_{rms}, given by

$$x_{rms} = \sqrt{\frac{1}{n}({x_1}^2 + \cdots + {x_n}^2)}, \tag{53}$$

where x_i corresponds to each of the n individual errors.

A stream function, determined by $\boldsymbol{\psi} = \frac{1}{2\pi N} sin(2\pi Nx) cos(2\pi Ny)\mathbf{k}$ is utilized in order to ensure that the resulting analytical velocity field is divergence-free. In this way, the derivation of $\boldsymbol{\psi}$, defined as $\mathbf{u} = \nabla \times \boldsymbol{\psi}$, gives the following periodic velocity field

$$\begin{aligned} u &= -sin(2\pi Nx) sin(2\pi Ny), \\ v &= -cos(2\pi Nx) cos(2\pi Ny), \\ w &= 0, \end{aligned} \tag{54}$$

which is solved in the three spatial directions and presents a maximum velocity magnitude of one. The test is performed on a cube of side 1.0×1.0×1.0 meshed by means of 9.2×10^3 hexahedral cells (Cartesian mesh) or 9.7×10^3 tetrahedral cells (unstructured mesh). Similarly to the previous test, Sec. 5.1, fluid with density $\rho_1 = 1\ kg/m^3$ occupies the entire cube except for a sphere of radius $R = 0.15$, which is fixed in the center of the domain and filled with a fluid of density $\rho_2 = 1000\ kg/m^3$.

In addition, instead of using meshes with different resolutions, the convergence study is performed by enlarging or reducing the wavelength of the

input sine functions, and consequently the radius of the centered sphere. In this way, the average mesh volume for both Cartesian and unstructured grids is calculated as $V_{avg} = \frac{1}{c}\sum_c V_c$, giving an average mesh spacing equal to $\Delta X_{avg} = \sqrt[3]{3V_{avg}} = 0.068$, whereas the effective length of the domain is defined as $L_{eff} = 1/N$, being N a variable integer value that is increased or decreased in order to enlarge or refine the effective mesh, respectively. In consequence, the relative mesh size is defined as $h = \Delta X_{avg}/L_{eff} = 0.068N$.

Convection accuracy errors are obtained for relative mesh sizes ranging from ≈ 0.1 to ≈ 0.5 and depicted in Fig. 6 —notice that results for the *sp* and *hspu* convection schemes are plotted with a single line since they are practically identical. The figure shows that, first, given a particular type of grid, *uw* errors are larger than *sp* and *hspu* ones for all relative mesh sizes, and second, for each convection scheme, errors are smaller on the Cartesian grid than on the unstructured one. Moreover, the order of accuracy of the different convection schemes have been calculated and collected in Tab. 2. These show that the three schemes are second-order accurate on Cartesian grids, while first- to second-order on unstructured meshes.

5.3. Spurious velocities around a spherical drop

In order to analyze the capability of the numerical framework to prevent, or diminish, spurious velocities, the test case of a drop first in equilibrium and later submerged in a swirling velocity field is considered. The drop is subjected to surface tension forces while gravity effects are neglected.

The set-up of the test is similar to the one proposed in Sec. 5.1. However, in this case the interface separating the two fluids is set free by coupling the VOF solver [8, 9] to the Navier-Stokes equations. In particular, a spherical drop of diameter $D = \pi$ is fixed in the center of a cubic domain of side 2π. Four different cases are analyzed corresponding to increasingly larger density ratio values $\mathbf{r}_\rho$. The surrounding fluid is of constant density $\rho_1 = 1$ kg/m^3, while the density of the drop ρ_2 is set to 1, 10, 100 and 1000 kg/m^3. Dynamic viscosity μ and gravity $\mathbf{g}$ are set to zero. Contrarily, the surface tension force, as introduced in Eq. 3, is characterized by a surface tension coefficient $\sigma = 7.3$ N/m, and by a curvature κ equal to $2/R$ in the case of a 3-D sphere. For the discretization of surface tension, a model based on the continuum surface force approach [38] is chosen. Therefore, for each cell c located at the interface, the surface tension is approximated as

$$\mathbf{T}_\sigma^c = \sigma\kappa \left(\frac{\nabla C_k}{\|\nabla C_k\|} \right)_c V_c, \tag{55}$$

where $\nabla C_k / \|\nabla C_k\|$ is the normalized gradient of the volume fraction scalar field C_k —in this case of the scalar field defining the surrounding fluid—, and V_c is the volume of the cell. A detailed description of the discretization of this force on 3-D unstructured meshes can be found in [3, 12, 39].

The domain is meshed exactly as in the 3-D vortex case: 6.6×10^4 triangular prisms, generated by extruding 30 times a 2-D grid discretized in 2.2×10^3 triangles. Once more, the time step is chosen to be $\Delta t = 1.0 \times 10^{-3}$

s and velocity free-slip conditions are imposed at X, Y and Z boundaries.

The test is initialized with a zero velocity field for each of the three convection schemes analyzed: symmetry-preserving (*sp*), upwind (*uw*) and hybrid symmetry-preserving upwind (*hspu*). Under these conditions, the velocity field along time should remain undisturbed, i.e., $\mathbf{u} = 0$. However, due to the appearance of spurious velocities at the cells located close to the interface, this is not the numerical solution obtained. Therefore, in order to measure the error in velocity, the following L_1 error norm is utilized

$$L_1(\mathbf{u}) = \frac{1}{n}\left(\|\hat{\mathbf{u}}_1\| + \cdots + \|\hat{\mathbf{u}}_n\|\right), \tag{56}$$

where $\hat{\mathbf{u}}_i$ corresponds to each of the n cell dimensionless velocities, evaluated as $\hat{\mathbf{u}}_i = \mathbf{u}_i\sqrt{\rho_2 D/\sigma}$.

The velocity L_1 errors for each convection scheme and density ratio are plotted in Fig. 7 versus dimensionless time $\hat{t} = t\sqrt{\sigma/(\rho_2 D^3)}$. As expected, for all cases, spurious velocities originate at cells located at the interface between fluids, and continuously propagate to the neighboring elements as time advances. Independently of the magnitudes, errors start at a zero value and increase with time for the three convection schemes. However, there is a clear difference between *sp* and *uw* and *hspu* errors. In the case of uniform density, $\mathbf{r}_\rho = 1$, the error for *sp* rapidly increases for $\hat{t} < 0.4$ first, and then continues smoothly increasing since no dissipation is introduced into the discrete solution to limit the spurious velocities. On the contrary, for the

uw and *hspu* schemes, the magnitude of the spurious currents stalls at $\hat{t} \simeq 0.2$ due to their low-dispersion characteristics. The contrast in behavior among the convection schemes significantly differs as the density ratio between fluids is increased. For example, for $\mathbf{r}_\rho = 1000$, the error magnitude for *uw* and *hspu* schemes is $\mathcal{O}(10^{-4})$, while it diverges for *sp*.

In order to assess the stabilization in a more realistic scenario, the spherical drop is introduced into the 3-D vortex velocity field described in Sec. 5.1. To impose a fast shape deformation, ρ_2 and A are set to 100 kg/m^3 and 1.0×10^{-1} m/s, respectively. In addition, the grid is refined to size $h = 0.1$. Results for the three convective schemes are shown in Fig. 8, and correspond to the evolution of the initial drop as dimensionless time $\hat{t} = tA/D$ advances. The figure clearly demonstrates the inability of the *sp* scheme to retain the shape of the deforming sphere due to the appearance of large spurious velocities at the surface. Differently, the solutions obtained with the *uw* and *hspu* are stable and qualitatively very similar —therefore, the transient evolution of the drop is shown by a unique sequence of snapshots. This result highlights the capability of the hybrid scheme to diminish spurious velocities around the interface, and therefore properly advect the surface separating the fluids. Particularly for this test, given the absence of turbulent motions, the two schemes provide a similar solution.

5.4. Atomization of a turbulent two-phase jet

In order to assess the capability of the *hspu* scheme to numerically simulate interfacial turbulent flow, the atomization of a two-phase jet is studied. The computational set-up is validated first by comparing against results reported by Fuster et al. [25]. Next, the advantages led by the adoption of the *hspu* scheme over the *uw* and *sp* are discussed.

5.4.1. Description of the case

The problem consists in the injection of two parallel high-speed streams of liquid l and gas g into an initially quiescent domain. A schematic representation of the jet evolution and geometrical dimensions are depicted in Fig. 9. Two dimensionless parameters characterize the problem. The Weber (We) number quantifies the ratio between fluid inertia and surface tension forces, while the Reynolds (Re) number accounts for the ratio of fluid inertia over viscous forces. For each fluid i, these are defined as

$$\mathrm{We}_i = \frac{\rho_i U_i^2 D}{\sigma} \qquad \mathrm{Re}_i = \frac{\rho_i U_i D}{\mu_i}, \tag{57}$$

where U_i is the inlet streamwise velocity, D is the liquid jet diameter, and σ is the surface tension coefficient. The physical properties of the fluids, namely ρ_i, μ_i and σ, as well as the resulting dimensionless parameters are reported in Tab. 3. Both fluids are injected with constant streamwise velocities starting from the left domain boundary. In addition, triggering of the instabilities responsible for transitioning from laminar to turbulent regime is forced by

assigning a random cross-stream velocity to the liquid phase at the inlet, with magnitude $V_l = [-0.1U_l : 0.1U_l]$. Finally, pressure is imposed at outlet such that appropriate outflow boundary conditions are obtained.

The first stages of the jet atomization are shown in Fig. 10 as function of dimensionless time tU_l/D. Zoomed figures (a) and (b) show the initial injection stages of the liquid jet. Figures (c) and (d) exhibit the appearance of interface instabilities that cause the formation and rupture of ligaments and the early spreading of droplets. Finally, jet swirling oscillation behavior is depicted in figures (e) and (f). These concatenated phenomena are comprehensively analyzed in the following subsections.

5.4.2. Numerical method

As indicated in the introduction, the low-dissipation convective scheme presented can be coupled to different interface-capturing methods. In order to demonstrate this capability, and motivated by a significant reduction in computational cost, the interface motion in this test is solved by means of the LS method presented in Balcázar et al. [3]. Moreover, the time step, instead of fixed to a particular value, is set free to dynamically adjust itself to the maximum value within the stability region — further details are given in the Appendix. Additionally, in order to reduce the computational requirements, an adaptive mesh refinement (AMR) strategy [40] is employed. As shown in Fig. 12 (Zoom B), the strategy consists in a dynamic refinement of the baseline mesh at the interfacial region. This refinement is essential

for capturing physical phenomena occurring at scales smaller than the initial mesh size, such as thin filaments or small drops. The base mesh is a uniform Cartesian grid with $\approx 5.0 \times 10^4$ cells. For this test, two levels of mesh refinement are utilized, i.e., the parent cell is divided at most into 16 sub-cells. Thus, at statistical steady-state conditions, the mesh reaches an average size of $\approx 2.3 \times 10^5$ elements, instead of the $\approx 8.2 \times 10^5$ elements that would be needed on a static mesh to obtain the same resolution. The refinement level is chosen after carrying out preliminary tests to determine the minimum mesh size necessary to obtain an acceptable convergence of the solution to the benchmark. Further details on the application of the AMR strategy to the jet atomization problem can be found in previous works [41, 42].

5.4.3. Validation and results

The case is discretely solved by utilizing the three convection schemes considered in this work: *sp*, *uw* and *hspu*. The first important outcome is that the *sp* scheme is not able to complete the calculation. Indeed, as previously demonstrated in Sec. 5.3, the inability of the scheme to contain spurious currents originated at the interface, results in the divergence of the numerical simulation in few time steps. On the other hand, calculations performed with the *uw* and *hspu* schemes are stable and their results are discussed below.

First, the use of the *hspu* convection scheme is validated by comparing the discrete results to the numerical data reported in [25]. For instance,

Fig. 11 shows the comparison of the time-averaged energy of the cross-stream normal velocity fluctuations $E_{v'} = (v')^2$ normalized by its inlet value $E_0 = (U_l)^2$. In particular, the figure shows the $E_{v'}/E_0$ profiles for three different inlet distances x/D. Due to the symmetry in geometry, only the profiles corresponding to the top-half part of the domain are represented. The results are compared to the same magnitudes measured in [25]. Regarding the first two distances, $x/D = 1.25$ and $x/D = 1.9$, present solution and benchmark match closely, thus, demonstrating a similar mechanism in the early growth of perturbations. At $x/D = 3.1$, where the process of disruption of the interface has taken place, despite showing an overall good agreement, the solutions result more distant. This is probably due to the different local definition of the mesh used in the representation of interface phenomena, that leads to a slightly different phenomenology of the unstable structure appearing after the core break-up.

The appearance of Kelvin-Helmholtz (KH) instabilities at the interface is due to the competition between shear forces, caused by the velocity difference of the two streams, and capillary stresses. This is in agreement with the reference work [25] and other studies regarding two-phase coaxial jets [5, 43, 44]. The KH instabilities are responsible for triggering the jet transition from laminar to turbulent regime. This phenomenon is captured by the intact jet profiles, $x/D = 1.25$ and 1.9, shown in Fig. 11, since E_i progressively rises in the interface proximity. In this zone, the fluctuations cause the appearance of waves at the interface that quickly grow, amplify and roll-up, breaking the

interface and spreading droplets downstream, as shown in Fig. 12 (Zoom A). The increase of the instability continues downstream, as the fluctuations are gradually transferred to the bulk of the fluids. Finally, perturbations cause the complete break-up of the liquid core, that fragments into droplets of several different sizes. The evolution of these physical mechanisms is depicted in Fig. 12.

The results obtained with the *uw* convection scheme are depicted in Fig. 13 where they are compared to *hspu* data. In detail, the figures compare the cross-stream kinetic energy of velocity fluctuations at entrance lengths $x/D = 1.25$ and 1.9. $E_{v'}$ evaluated with *uw* is slightly lower than *hspu*, due to the dissipative nature of the method, which causes a partial attenuation of kinetic energy also in the core of the liquid phase. However, results are comprehensibly similar, demonstrating an equivalent representation of the KH instability mechanism for the two schemes. As it will be demonstrated in the next subsection, Sec 5.4.4, this similarity in behavior is not encountered for the energy spectra of the downstream turbulent region.

5.4.4. Energy spectra

Following the complete breakdown of the liquid-phase core, a downstream turbulent dispersion of droplets is observed. After ≈ 60 dimensionless time units tU_l/D, the two-phase dispersed system reaches a statistical steady state regime with the overall wake fluctuating under a constant vortex shedding frequency f_{VS}. In this context, the analysis of the flow energy spectrum

allows a more complete knowledge of its turbulent behavior and a further verification of the *hspu* scheme. The spectra have been calculated from the time series of the vertical velocity v over a large exhibition period of ≈ 25 shedding cycles.

The velocity probes are located at different inlet distances x/D, and at a vertical position equal to the inlet interface y-axis value y_{int}. This vertical position of the probes ensures a better capturing of the interface fluctuations. A satisfactory description of the jet turbulent behavior can be drawn from the analysis of the results obtained on two probes. The first, S1, is placed in the zone of the earliest interface instabilities ($x/D = 2$), where the disturbances have not yet broken the liquid core, whereas the second, S2, is located at $x/D = 6$, where the core is partially broken and the vortex shedding has begun to drag the structures downstream —see position of the probes in Fig. 12.

Segments of the velocity signals collected by the probes at statistical steady state conditions are plotted in Fig. 14. The *hspu* velocity signal of probe S1, reported in Fig. 14(a), shows much more regular oscillations than the *uw* signal, and a notably higher value of root-mean-square velocity. In the case of probe S2 —see Fig. 14(b) —, the *uw* signal fluctuates more strongly, but oscillations are still less regular and energetic than the *hspu* ones.

The described velocity signals are post-processed by using the Lomb periodogram technique [45] to yield the turbulent energy spectra, reported in

Fig. 15. The plots depict the dimensionless energy of cross-stream velocity fluctuations, $E_{v'}/E_0$, as function of fD/U_l. All the curves are compared to the (-3)-slope, characteristic of the direct energy cascade in 2-D turbulence [46]. Regarding the *hspu* scheme, the spectra show the same dominant peak for both S1 and S2 probes, Figs. 15(a) and 15(c), corresponding to the vortex shedding Strouhal number $\mathrm{St_{VS}} = f_{\mathrm{VS}}D/U_l = 0.27$. The existence of a strong dominant frequency is confirmed by the appearance of harmonic peaks — up to the third in probe S1, and up to the fourth in probe S2. In probe S1, a peak associated to the KH instability is visible at $f_{\mathrm{KH}}D/U_l \approx 1.0$. Despite being responsible for the laminar to turbulent transition, KH remains embedded in the vortex shedding frequency, and becomes barely distinguishable. The slope of the energy cascade is well represented in both probes.

On the other hand, referring to the *uw* scheme, two energy peaks are detected by both probes, at $\mathrm{St_{VS1}} = 0.24$ and $\mathrm{St_{VS2}} = 0.31$, as shown in Figs. 15(b) and 15(d). These are responsible for an irregular fluid shedding, previously suggested by the uneven velocity signal shown in Fig. 14. Indeed, the dissipative nature of the scheme makes the wake more fragmented and driven by different fluctuation frequencies. Conversely, the foot print of KH instabilities at the interface is well captured by probe S1, at $\mathrm{f}_{KH}D/U_l \approx 0.9$, due to the absence of a strong dominant shedding frequency.

In conclusion, the *hspu* scheme proves to be effective in the simulation of turbulent jet atomization, as it is able to properly resolve the energy cascade and to reproduce the vortex shedding effect. Moreover, its adoption

has many advantages in comparison to other existing schemes. For instance, *hspu* solves the poor numerical stability shown by *sp* at liquid-gas interfaces. On the other hand, it provides a proper transport of kinetic energy in the vortex shedding mechanism, thus, overcoming the inability of *uw* to accurately solve turbulent flows. Indeed, the utilization of the *sp* scheme for the cells located in the bulk of the fluids guarantees the discrete convective operator to be locally skew-symmetric and, therefore, the correct conservation of mass, momentum and kinetic energy [27].

6. Conclusions

In this work, a low-dissipation and low-dispersion discretization for the numerical simulation of turbulent interfacial flow is analyzed. The scheme is designed to minimize the amount of artificial dissipation introduced into the discrete system, while manages to limit the growth of spurious currents. In addition, as demonstrated in the series of tests performed, the hybrid convection scheme proposed can be coupled to different interface-capturing methods.

The theoretical analysis presented in Secs. 3 and 4 demonstrates that the scheme is conservative except for the subgroup of cells found in the vicinity of the interface, where a controlled amount of dissipation is introduced to diminish spurious flows. This feature is confirmed by the numerical results of a 3-D vortex presented in Sec. 5.1. The same test shows that the overall kinetic-energy dissipation is kept to a level well lower than classic dissipative

schemes. The spatial accuracy of the method is numerically analyzed in Sec. 5.2, where it is shown to be second-order accurate on Cartesian grids and first-order on unstructured 3-D meshes.

The localized injection of dissipation allows an effective control of the spurious currents growth, which provides enhanced stability to the numerical method. Indeed, as demonstrated in the spherical drop test in Sec. 5.3, spurious flows grow unbounded when using purely conservative discretizations, whereas remain contained to small values in the case of utilizing the hybrid convection scheme. This behavior is further corroborated by obtaining a proper interface advection when the sphere is placed in a swirling velocity field.

The performance of the numerical framework in a complete multiphase turbulent scenario has been tested by solving a liquid-gas atomizing jet. On the one hand, the test demonstrates that the controlled dissipation added to the interfacial region is sufficient to stabilize the numerical simulation. On the other hand, the results expose that, unlike pure dissipative schemes, the hybrid convection approach presented in this work is able to properly represent the underlying physics of turbulent flow. Consequently, the inability of a pure dissipative method to properly transport swirling structures is overcome.

Appendix. Time step evaluation

In the case of high-Reynolds-number flow, if the equations of fluid motion, Eqs. 1 and 2, are explicitly integrated in time — which is generally less expensive than using implicit methods [47] —, the time step value is limited by the stability of the convective term. Therefore, applying stability theory to the matrix resulting from multiplying the discrete convective operator by time step, $\Delta t\, \mathbf{C}(\rho\mathbf{u})$, the region of absolute stability can be determined on the complex plane by imposing

$$\Delta t |\lambda_i^C| \leq 1 \qquad \forall i = 1, ..., m, \tag{58}$$

with $\lambda_i^C \in \mathbb{I}$ the eigenvalues of the $m \times m$ convective operator matrix.

The solution of large eigenvalue problems is extraordinary time-consuming, particularly in the case of Eq. 58, since $\mathbf{C}(\rho\mathbf{u})$ changes every time step. In fact, the calculation of the eigenvalues requires an amount of computational resources similar to that of solving the discrete system. Thus, this is not a real option. Instead, as proposed in [48], a more practical approach is to bound them by means of the Gershgorin circle theorem [49], written as

$$|\lambda_i^C - c_{ii}| \leq \sum_{j \neq i} |c_{ij}| \qquad \forall i = 1, ..., m, \tag{59}$$

where c_{ii} and c_{ij} are, respectively, the diagonal and off-diagonal elements of the discrete convective matrix defined in Eqs. 40 and 41. Hence, the

maximum time step within the stability region results from considering the largest eigenvalue in Eq. 59, defined as

$$|\lambda^{C}_{max}| \leq max\left[|c_{ii}| + \sum_{j \neq i}|c_{ij}|\right] \qquad \forall i = 1, ..., m. \tag{60}$$

Acknowledgments

This work has been financially supported by the Ministerio de Economía y Competitividad, Secretaría de Estado de Investigacíon, Desarrollo e Innovacíon, Spain (ENE-2014-60577-R, ENE2015-70672-P), a FI Grant by AGAUR (Generalitat de Catalunya), and by Termo Fluids S.L.

References

[1] C. E. Brennen, Fundamentals of multiphase flow, Cambridge University Press, 2005.

[2] C. S. Peskin, Numerical analysis of blood flow in the heart, Journal of computational physics 25 (1977) 220–252.

[3] N. Balcázar, L. Jofre, O. Lehmkuhl, J. Castro, J. Rigola, A finite-volume/level-set method for simulating two-phase flows on unstructured grids, International Journal of Multiphase Flow 64 (2014) 55–72.

[4] R. Scardovelli, S. Zaleski, Direct numerical simulation of free-surface and interfacial flow, Annual Review of Fluid Mechanics 31 (1999) 567–603.

[5] M. Gorokhovski, M. Herrmann, Modeling primary atomization, Annual Review of Fluid Mechanics 40 (2008) 343–366.

[6] C. W. Hirt, B. D. Nichols, Volume of fluid (VOF) method for the dynamics of free boundaries, Journal of Computational Physics 39 (1981) 201–225.

[7] P. Liovic, M. Rudman, J.-L. Liow, D. Lakehal, D. Kothe, A 3D unsplit-advection volume tracking algorithm with planarity-preserving interface reconstruction, Computers & Fluids 35 (2006) 1011–1032.

[8] L. Jofre, O. Lehmkuhl, J. Castro, A. Oliva, A 3-D volume-of-fluid advection method based on cell-vertex velocities for unstructured meshes, Computers & Fluids 94 (2014) 14–29.

[9] L. Jofre, R. Borrell, O. Lehmkuhl, A. Oliva, Parallel load balancing strategy for volume-of-fluid methods on 3-D unstructured meshes, Journal of Computational Physics 282 (2015) 269–288.

[10] S. Osher, J. A. Sethian, Fronts propagating with curvature-dependent speed: algorithms based on Hamilton-Jacobi formulations, Journal of Computational Physics 79 (1988) 12–49.

[11] E. Olsson, G. Kreiss, A conservative level set method for two phase flow, Journal of Computational Physics 210 (2005) 225–246.

[12] N. Balcázar, O. Lehmkuhl, L. Jofre, J. Rigola, A. Oliva, A coupled

volume-of-fluid/level-set method for simulation of two-phase flows on unstructured meshes, Computers & Fluids 124 (2016) 12 –29.

[13] B. Lafaurie, C. Nardone, R. Scardovelli, S. Zaleski, G. Zanetti, Modelling merging and fragmentation in multiphase flows with SURFER, Journal of Computational Physics 113 (1994) 134–147.

[14] Y. Renardy, M. Renardy, PROST: a parabolic reconstruction of surface tension for the volume-of-fluid method, Journal of Computational Physics 183 (2002) 400–421.

[15] S. Zahedi, M. Kronbichler, G. Kreiss, Spurious currents in finite element based level set methods for two-phase flow, International Journal for Numerical Methods in Fluids 69 (2012) 1433–1456.

[16] F. Denner, B. G. van Wachem, On the convolution of fluid properties and surface force for interface capturing methods, International Journal of Multiphase Flow 54 (2013) 61–64.

[17] M. M. François, S. J. Cummins, E. D. Dendy, D. B. Kothe, J. M. Sicilian, M. W. Williams, A balanced-force algorithm for continuous and sharp interfacial surface tension models within a volume tracking framework, Journal of Computational Physics 213 (2006) 141–173.

[18] A. Y. Tong, Z. Wang, A numerical method for capillarity-dominant free surface flows, Journal of Computational Physics 221 (2007) 506–523.

[19] A. J. Chorin, A numerical method for solving incompressible viscous flow problems, Journal of Computational Physics 2 (1967) 12–26.

[20] A. Di Mascio, R. Broglia, R. Muscari, On the application of the single-phase level set method to naval hydrodynamic flows, Computers & Fluids 36 (2007) 868–886.

[21] X. Lv, Q. Zou, Y. Zhao, D. Reeve, A novel coupled level set and volume of fluid method for sharp interface capturing on 3D tetrahedral grids, Journal of Computational Physics 229 (2010) 2573–2604.

[22] E. Schillaci, L. Jofre, N. Balcázar, O. Lehmkuhl, A. Oliva, A level-set aided single-phase model for the numerical simulation of free-surface flows on unstructured meshes, Computers & Fluids 140 (2016) 97–110.

[23] S. Popinet, An accurate adaptive solver for surface-tension-driven interfacial flows, Journal of Computational Physics 228 (2009) 5838–5866.

[24] R. Löhner, C. Yang, E. Onate, Simulation of flows with violent free surface motion and moving objects using unstructured grids, International Journal for Numerical Methods in Fluids 53 (2007) 1315–1338.

[25] D. Fuster, A. Bagué, T. Boeck, L. Le Moyne, A. Leboissetier, S. Popinet, P. Ray, R. Scardovelli, S. Zaleski, Simulation of primary atomization with an octree adaptive mesh refinement and vof method, International Journal of Multiphase Flow 35 (2009) 550–565.

[26] R. Verstappen, A. Veldman, Symmetry-preserving discretization of turbulent flow, Journal of Computational Physics 187 (2003) 343–368.

[27] L. Jofre, O. Lehmkuhl, J. Ventosa, F. X. Trias, A. Oliva, Conservation properties of unstructured finite-volume mesh schemes for the Navier-Stokes equations, Numerical Heat Transfer, Part B: Fundamentals 65 (2014) 53–79.

[28] X. Trias, O. Lehmkuhl, A. Oliva, C. Pérez-Segarra, R. Verstappen, Symmetry-preserving discretization of navier-stokes equations on collocated unstructured grids, Journal of Computational Physics 258 (2014) 246–267.

[29] D. Fuster, An energy preserving formulation for the simulation of multiphase turbulent flows, Journal of Computational Physics 235 (2013) 114–128.

[30] A. E. Veldman, K.-W. Lam, Symmetry-preserving upwind discretization of convection on non-uniform grids, Applied Numerical Mathematics 58 (2008) 1881–1891.

[31] S. Pirozzoli, Numerical methods for high-speed flows, Annual review of fluid mechanics 43 (2011) 163–194.

[32] F. X. Trias, A. Gorobets, A. Oliva, A simple approach to discretize the viscous term with spatially varying (eddy-) viscosity, Journal of Computational Physics 253 (2013) 405–417.

[33] L. Jofre, O. Lehmkuhl, N. Balcázar, J. Castro, J. Rigola, A. Oliva, Conservative discretization of multiphase flow with high density ratios, WIT Transactions on Engineering Sciences 82 (2014) 153–164.

[34] Y. Morinishi, T. Lund, O. Vasilyev, P. Moin, Fully conservative higher order finite difference schemes for incompressible flow, Journal of Computational Physics 143 (1998) 90–124.

[35] F. N. Felten, T. S. Lund, Kinetic energy conservation issues associated with the collocated mesh scheme for incompressible flow, Journal of Computational Physics 215 (2006) 465–484.

[36] G. Fishpool, M. Leschziner, Stability bounds for explicit fractional-step schemes for the Navier-Stokes equations at high Reynolds number, Computers & Fluids 38 (2009) 1289–1298.

[37] O. Lehmkuhl, C. Pérez-Segarra, R. Borrell, M. Soria, A. Oliva, TERMOFLUIDS: A new parallel unstructured CFD code for the simulation of turbulent industrial problems on low cost PC cluster, in: Parallel Computational Fluid Dynamics 2007, Springer, 2009, pp. 275–282.

[38] J. Brackbill, D. B. Kothe, C. Zemach, A continuum method for modeling surface tension, Journal of Computational Physics 100 (1992) 335–354.

[39] N. Balcázar, J. Rigola, J. Castro, A. Oliva, A level-set model for thermocapillary motion of deformable fluid particles, International Journal of Heat and Fluid Flow 62 (2016) 324–343.

[40] O. Antepara, O. Lehmkuhl, R. Borrell, J. Chiva, A. Oliva, Parallel adaptive mesh refinement for large-eddy simulations of turbulent flows, Computers & Fluids 110 (2014) 48–61.

[41] E. Schillaci, O. Antepara, O. Lehmkuhl, N. Balcázar, A. Oliva, Effectiveness of adaptive mesh refinement strategies in the DNS of multiphase flows, in: Proceedings of International Symposium Turbulent Heat and Mass Transfer VIII, 2015.

[42] E. Schillaci, O. Lehmkuhl, O. Antepara, A. Oliva, Direct numerical simulation of multiphase flows with unstable interfaces, Journal of Physics: Conference Series 745 (2016).

[43] J. Lasheras, E. Hopfinger, Liquid jet instability and atomization in a coaxial gas stream, Annual Review of Fluid Mechanics 32 (2000) 275–308.

[44] H. Grosshans, A. Movaghar, L. Cao, M. Oevermann, R.-Z. Szász, L. Fuchs, Sensitivity of VOF simulations of the liquid jet breakup to physical and numerical parameters, Computers & Fluids 136 (2016) 312–323.

[45] N. R. Lomb, Least-squares frequency analysis of unequally spaced data, Astrophysics and space science 39 (1976) 447–462.

[46] R. H. Kraichnan, Inertial ranges in two-dimensional turbulence, Physics of Fluids 10 (1967) 1417–1423.

[47] R. Verstappen, A. Veldman, Direct numerical simulation of turbulence at lower costs, Journal of Engineering Mathematics 32 (1997) 143–159.

[48] F. X. Trias, O. Lehmkuhl, A self-adaptive strategy for the time integration of Navier-Stokes equations, Numerical Heat Transfer, Part B: Fundamentals 60 (2011) 116–134.

[49] S. Gerschgorin, Über die abgrenzung der eigenwerte einer matrix, Fiziko-Matematicheskaya Nauka 7 (1931) 749–754.

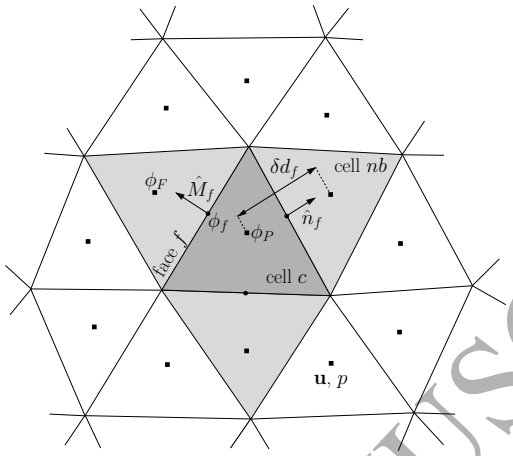

Figure 1: Arrangement of variables and notation for the collocated framework and convection scheme on a 2-D unstructured mesh. The schematic representation shows the collocated position of velocity $\mathbf{u}$ and pressure p. The cell c where the discretization is analyzed is shown in dark gray, while the face-neighboring cells nb are depicted in light gray, with an example of normal outward unit vector $\hat{\mathbf{n}}_f$ and distance δd_f between centroids. An example of a face f where the $\boldsymbol{\phi}_f$ is evaluated, together with the corresponding $\hat{M}_f$, $\boldsymbol{\phi}_P$ and $\boldsymbol{\phi}_F$ values, is illustrated.

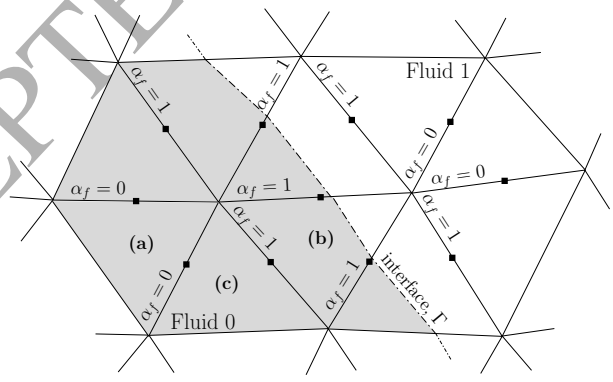

Figure 2: Example of the values taken by α_f at different faces according to the interface position when using the VOF method as interface capturer.

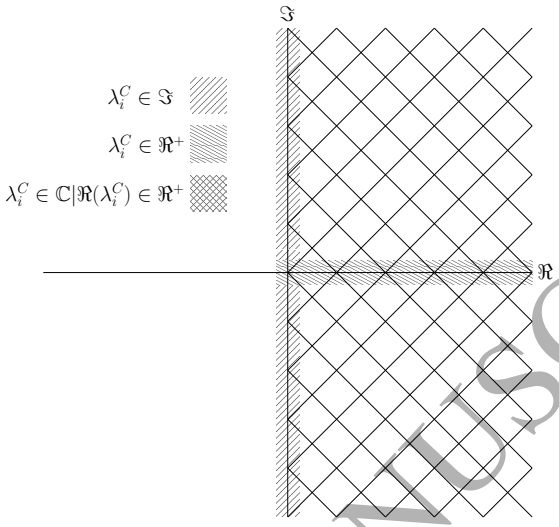

Figure 3: Distribution on the real-imaginary diagram of the eigenvalues corresponding to the discrete convective matrix. Three different cases are depicted depending on the values taken by α_f.

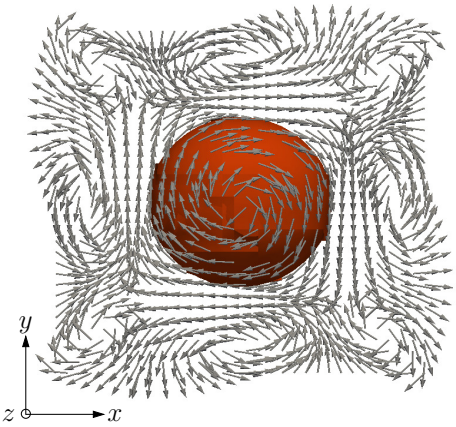

Figure 4: 3-D vortex: frontal (xy-plane) view of the flow field and interface location. Velocity vectors are displayed in gray while the high-density sphere is shown in orange.

$\mathbf{r}_\rho$	*sp* $\mathcal{O}$(-)	*uw* $\mathcal{O}$(-)	*hspu* $\mathcal{O}$(-)
1	10^{-14}	10^{-8}	10^{-9}
10	10^{-13}	10^{-7}	10^{-8}
100	10^{-12}	10^{-6}	10^{-7}
1000	10^{-11}	10^{-5}	10^{-6}

Table 1: 3-D vortex: order of magnitude of kinetic energy variation by the convection term, $|\nabla \cdot \mathbf{u}(\frac{1}{2}\rho\mathbf{u} \cdot \mathbf{u})|$ obtained by using the *sp*, *uw* and *hspu* schemes. The quantity is evaluated for increasingly larger density ratios.

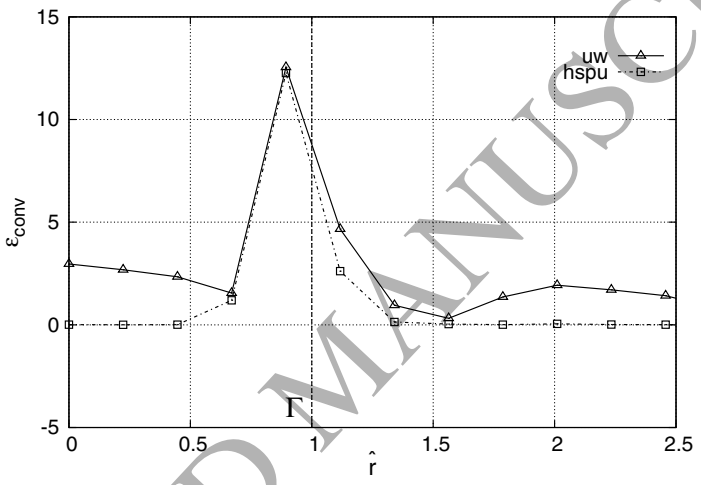

Figure 5: 3-D vortex: relative error of convection kinetic energy variation ϵ_{conv} along the cells that lay on the line from the sphere's center to a corner of the domain as a function of dimensionless radius $\hat{r}$. The interface location is indicated by Γ.

Scheme	Cartesian	Unstructured
sp, *hspu*	2.69	1.53
uw	1.88	1.43

Table 2: Order of accuracy of the different convection schemes (*sp*, *uw* and *hspu*) on both mesh types (Cartesian and unstructured).

	U_i[m/s]	ρ_i[kg/m^3]	μ_i [Pa·m]	σ [N/m]	Re$_i$	We$_i$
liquid	20	1000	5×10^{-4}	0.03	16000	5332
gas	100	100	1.7×10^{-5}		235000	13000

Table 3: Atomization of a two-phase jet: liquid and gas physical properties and dimensionless parameters.

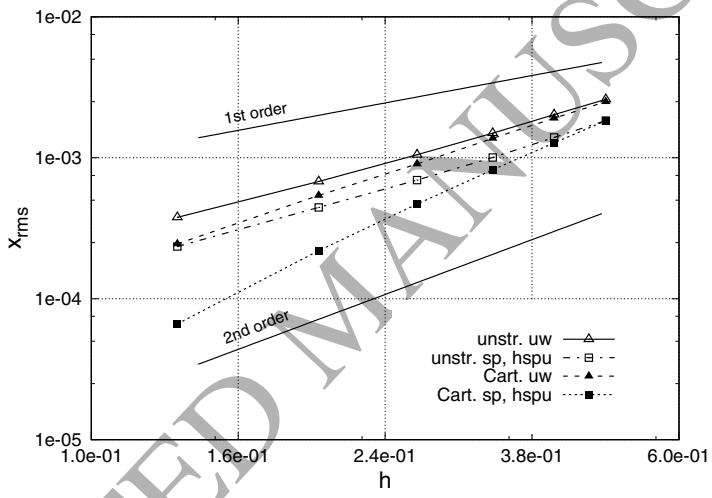

Figure 6: Exact sinusoidal function: convection scheme error x_{rms} versus relative mesh size h for the different convection schemes (*sp*, *uw* and *hspu*) and mesh types (Cartesian and unstructured). First- and second-order slopes are also indicated.

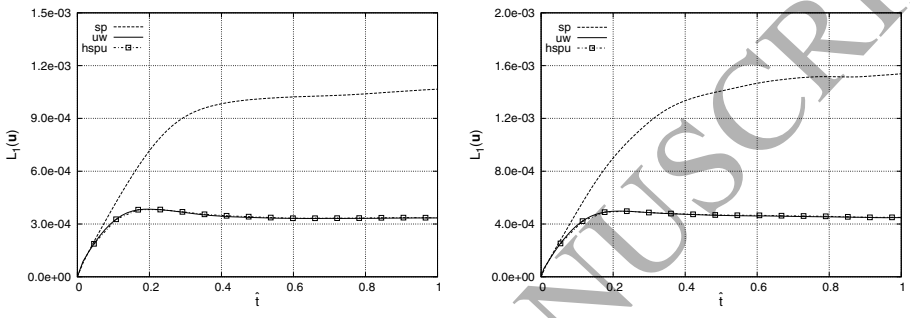

(a) $\mathbf{r}_\rho = 1$

(b) $\mathbf{r}_\rho = 10$

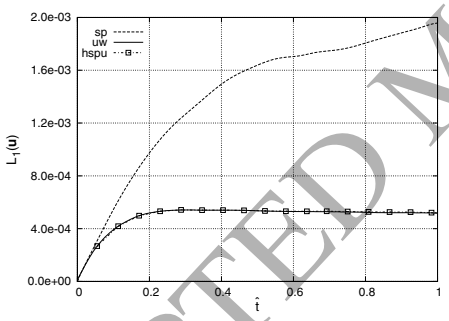

(c) $\mathbf{r}_\rho = 100$

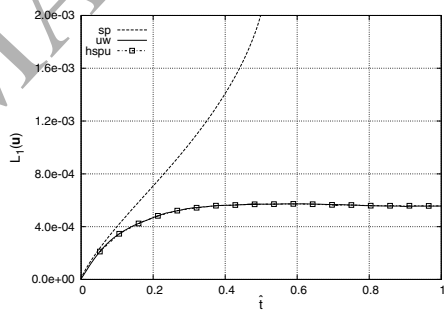

(d) $\mathbf{r}_\rho = 1000$

Figure 7: Spherical drop in equilibrium: velocity errors L_1 versus dimensionless time $\hat{t}$ for the three convection schemes analyzed (*sp*, *uw* and *hspu*) and for increasingly larger density ratios $\mathbf{r}_\rho$.

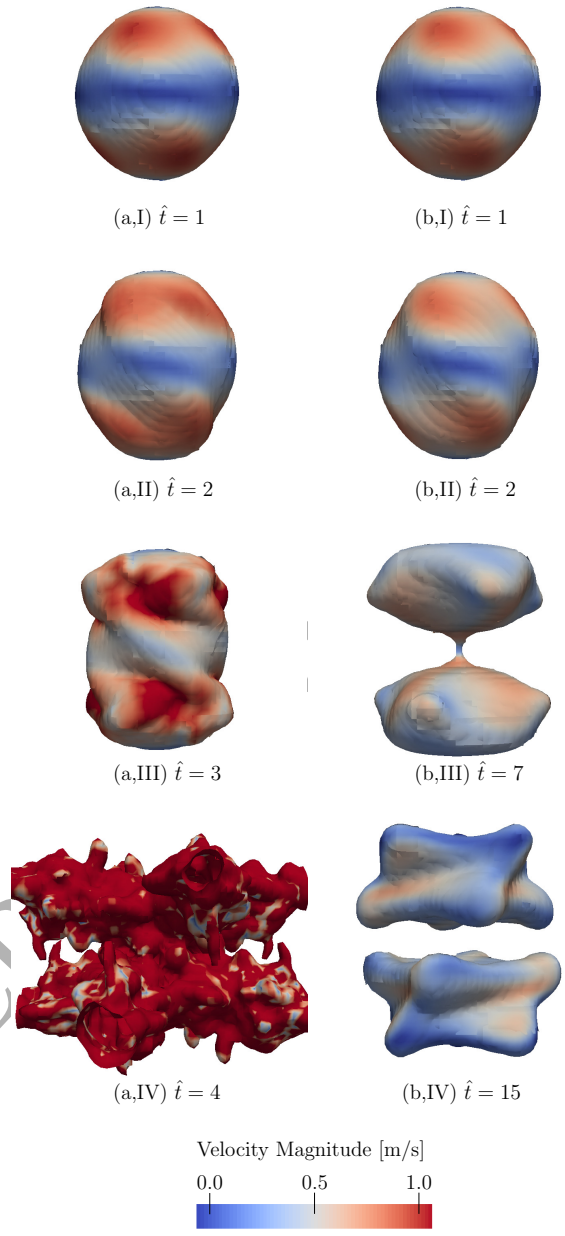

(a) *sp* (b) *uw*, *hspu*

Figure 8: Spherical drop under swirling action: time evolution (top to bottom) of the sphere for the *sp* (left), *uw* and *hspu* (right) convection schemes. The interface is colored according to the velocity magnitude.

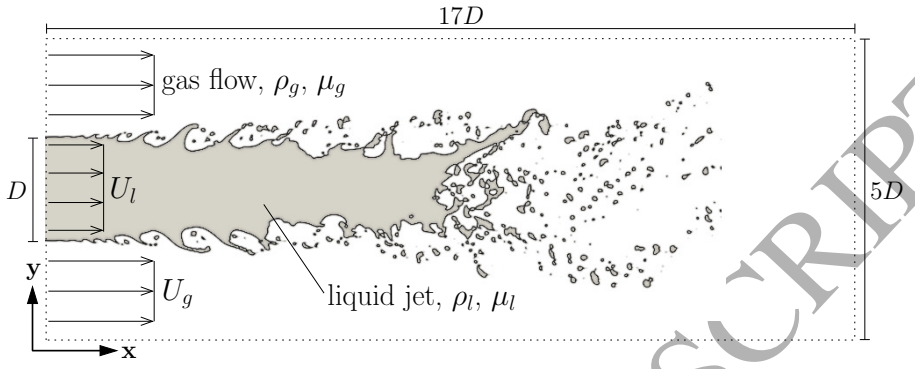

Figure 9: Atomization of a two-phase jet: schematic representation of the liquid jet test indicating the flow configuration and geometrical parameters.

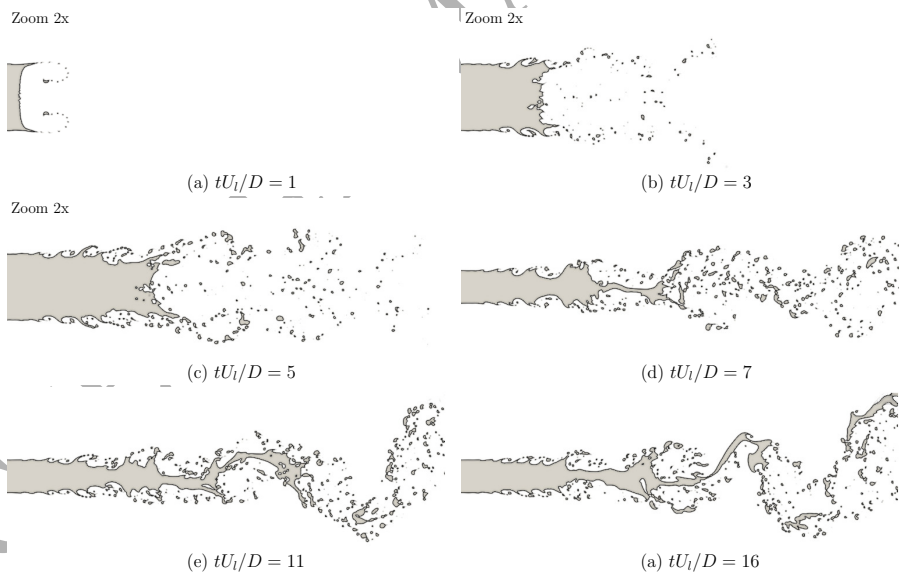

Figure 10: Atomization of a two-phase jet: initial stages of the liquid atomization process.

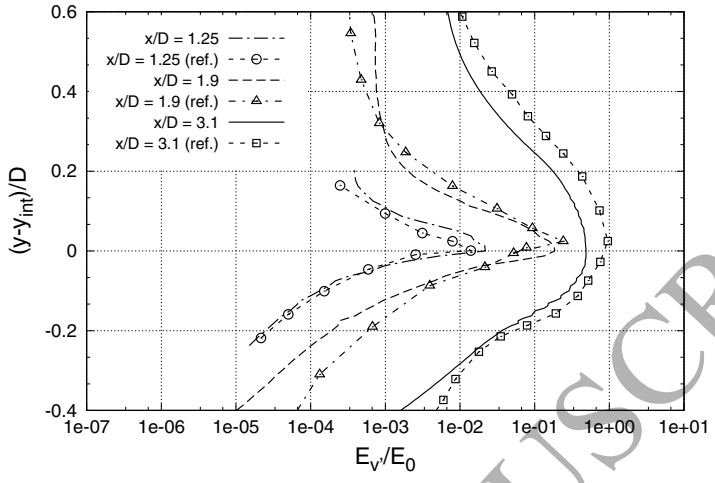

Figure 11: Atomization of a two-phase jet: energy of the cross-stream normal velocity fluctuations $E_{v'} = (v')^2$ normalized by its inlet value E_0 and evaluated at different distances from the inlet x/D. Present results are compared to reference data reported in [25]. The *hspu* convection scheme is used to discretize the convection term. Parameter y_{int} corresponds to the value of the interface vertical position at inlet.

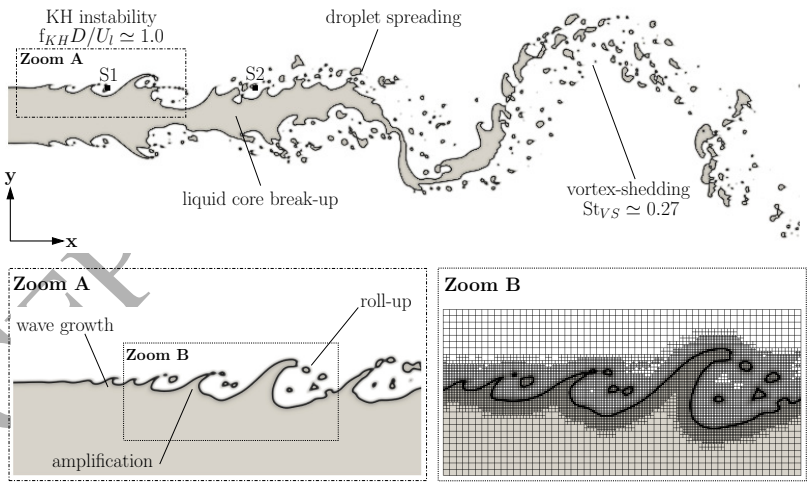

Figure 12: Atomization of a two-phase jet: visualization of the primary and secondary stages of the atomization process obtained from the numerical simulation. The position of velocity probes $(S1, S2)$ is indicated. In Zoom A, a detail of the waves evolution at the interface is shown. Zoom B is an example of the refined mesh achieved with the AMR strategy at the interface.

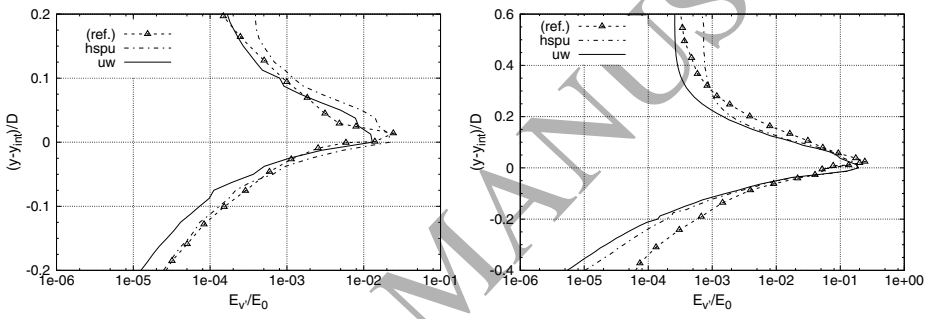

(a) x/D=1.25 (b) x/D=1.9

Figure 13: Atomization of a two-phase jet: energy of the cross-stream normal velocity fluctuations $E_{v'}/E_0$ measured at different distances from the inlet x/D using the *uw* and *hspu* convection schemes. Results are compared to numerical data reported in reference [25].

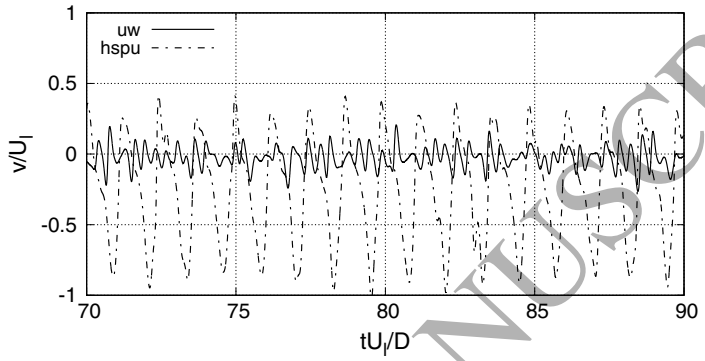

(a) Probe S1

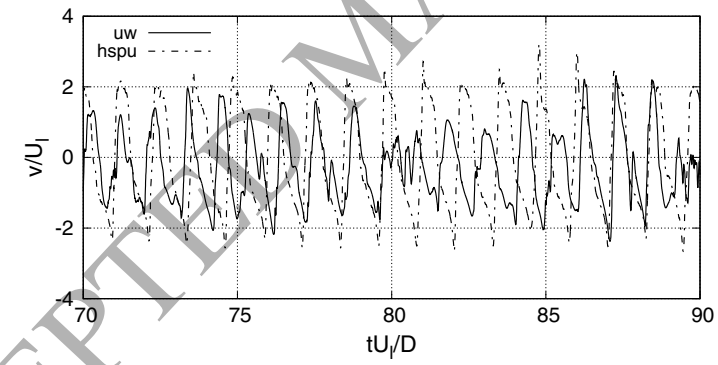

(b) Probe S2

Figure 14: Atomization of a two-phase jet: dimensionless vertical velocity v/U_l measured at probes S1 and S2 using the *uw* and *hspu* schemes.

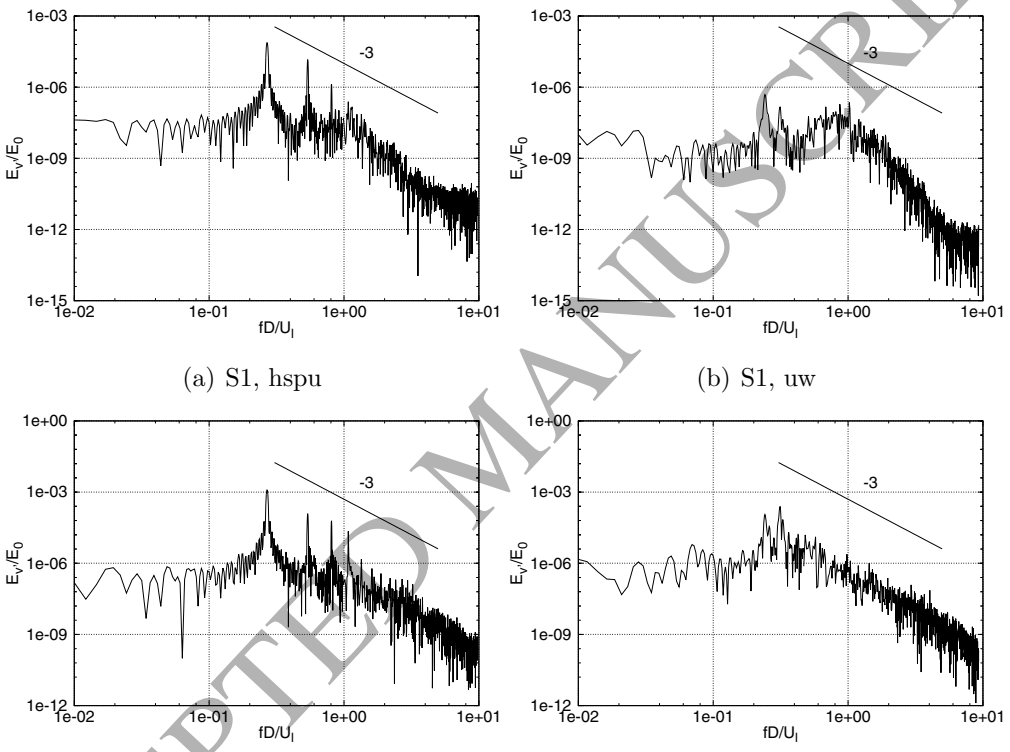

(a) S1, hspu

(b) S1, uw

(c) S2, hspu

(d) S2, uw

Figure 15: Atomization of a two-phase jet: energy spectra $E_{v'}/E_0$ measured at probes S1 and S2 using the *uw* and *hspu* convection schemes.